frontiers | Frontiers in Built Environment

TYPE Original Research
PUBLISHED 25 September 2024
DOI 10.3389/fbuil.2024.1454266

Check for updates

OPEN ACCESS

EDITED BY
Hoang Bao Khoi Nguyen,
University of South Australia, Australia

REVIEWED BY
Christos Vrettos,
University of Kaiserslautern, Germany
Haizuo Zhou,
Tianjin University, China

*CORRESPONDENCE
Andreas-Nizar Granitzer,
✉ andreas-nizar.granitzer@tugraz.at

RECEIVED 24 June 2024
ACCEPTED 09 September 2024
PUBLISHED 25 September 2024

CITATION
Granitzer A-N, Felic H, Leo J, Stastny A and Tschuchnigg F (2024) Numerical investigation of pile foundation systems employing an enhanced embedded finite element.
Front. Built Environ. 10:1454266.
doi: 10.3389/fbuil.2024.1454266

Numerical investigation of pile foundation systems employing an enhanced embedded finite element

Andreas-Nizar Granitzer[1]*, Haris Felic[1], Johannes Leo[1], Alexander Stastny[1,2] and Franz Tschuchnigg[1]

[1]Computational Geotechnics Group, Institute for Soil Mechanics, Foundation Engineering and Computational Geotechnics, Graz University of Technology, Graz, Austria, [2]DB InfraGO AG, Munich, Germany

The design of large-scale pile foundation systems is routinely assisted by finite element simulations. To a large extent, both the modeling and the computational effort of such analyses are governed by the adopted pile modeling technique. The traditional approach to this problem fully resolves the pile and soil domain employing solid elements, resulting in considerable meshing constraints and high simulation runtimes that may be regarded as unbearable for many practical purposes. As an attractive alternative to circumvent these obstacles, embedded FE models have become increasingly popular in solving this modeling task, mainly due to their flexible meshing procedure and significantly enhanced runtime efficiency. In a preceding contribution, the authors have proposed an extended formulation that provides a rigorous framework to capture soil-structure interaction effects at the physical soil-pile contacts. As a key feature, the implemented combined soil-pile coupling scheme explicitly accounts for endpoint interaction. However, validation studies have been constrained to single pile analyses to date. The present work expands this validation scope to large-scale boundary value problems involving multiple piles and investigates the model performance based on three different case studies. The results are compared to both, measurements and numerical benchmark solutions and provide exclusive insight into the numerical fidelity of the developed embedded FE model, with a view to increasing its potential for take-up in engineering practice.

KEYWORDS

embedded finite element, pile, foundation, integral bridge, high-rise building

1 Introduction

Pile foundation systems are routinely used for overcoming the challenges of founding large-scale structures, such as high-rise buildings (Tschuchnigg and Schweiger, 2013) or integral bridges (Stastny et al., 2024), in soft soil areas (Poulos and Davis, 1980). Related structures are typically subjected to a combination of vertical, lateral and overturning forces, and have to satisfy limit state requirements concerning their overall stability, serviceability and structural components (DGGT, 2014). A major concern in such analyses is the rigorous treatment of interactions between the structure, the piles and the ground (Hanisch et al., 2002). While simplified design strategies based on empirical or analytical methods remain an integral part in the preliminary design of pile foundation systems, they have an implicit range of applicability that is often disregarded (Sheil et al., 2019); interested readers may refer to Poulos (2010) which highlights pitfalls resulting from an inconvenient selection of related methods.

In comparison, three-dimensional (3D) finite element analyses (FEA) have a relatively higher potential to capture the complex structural behavior of pile foundation systems, particularly in the presence of inhomogeneous soil conditions (Marzouk et al., 2024), non-symmetric geometries (Granitzer et al., 2021) and complex loading paths (Staubach et al., 2023). Nevertheless, in many cases, the use of FEA is limited by the available computational resources for solving boundary value problems (BVPs). In this context, a particularly relevant factor is the pile modeling approach, as it significantly influences the number of degrees of freedom (DOFs) in the underlying system of equations that has to be solved. The standard FE approach (SFEA) to this modeling task incorporates a fully 3D surface-to-surface mesh tying problem between the surfaces of the pile domain (Ω^p) and the soil domain (Ω^s), that is, the pile volume is explicitly cut out of the surrounding soil volume; compare (Tschuchnigg and Schweiger, 2015; Abu-Farsakh et al., 2018; Steinbrecher et al., 2020). This pile modeling technique rigorously captures the geometry of the physical pile-to-soil coupling problem, hence it is expected to provide very accurate solutions, also in close vicinity to the pile-soil interface. The SFEA is therefore commonly used as a numerical benchmark to assess the credibility of novel pile formulations (Granitzer and Tschuchnigg, 2021). However, the reader should notice that, within the range of practically relevant applications, this pile modeling technique requires local refinement of the spatial mesh topology to adequately capture the relatively steep gradients in the field variables (e.g., stresses and displacements), which are typically localized close to the piles (Trochanis et al., 1991). This mesh constraint results in a high number of DOFs that scales with the number of discretized piles, and inevitably triggers high computation costs (Steinbrecher et al., 2022b). In addition, it commonly prohibits the use of the SFEA for iterative design procedures, which greatly benefit from the arbitrary positioning of structural elements inside the analysis domain; compare Di Prisco et al., 2020; Jürgens et al., 2022.

To circumvent these obstacles inherent to the SFEA, the use of embedded FE models has attracted significant interest in the field of computational geotechnics, particularly for the analysis of bored piles with insignificant soil disturbance caused by pile installation. This concern is underlined by their wide diffusion in commercial finite element (FE) codes, among which ZSoil 3D, RS3, Diana 3D and PLAXIS 3D (Granitzer and Tschuchnigg, 2021). As a key characteristic of embedded FE models, Ω^p is represented through a dimensionally reduced one-dimensional (1D) FE (Öchsner and Merkel, 2018), instead of discretizing the pile geometry details in 3D space. Relative merits of embedded FE models can be further attributed to the incorporation of mixed-dimensional 1D-to-3D coupling schemes established between Ω^p and Ω^s (each equipped with distinct DOFs), which describes the coupling conditions at the continuum formulation level (Turello et al., 2017; Turello et al., 2019). Essentially, this feature allows to formulate the coupling conditions between Ω^p and Ω^s on non-matching meshes (that is, the contacting bodies are independently discretized) and facilitates flexible mesh generation and pile modeling procedures.

Building on the seminal works of Ngo and Scodelis (1967) and Phillips and Zienkiewicz (1976) carried out in the field of structural concrete, a number of researchers have contributed to the gradual evolution of embedded FE models for the numerical analysis of geotechnical problems involving piles (Waas and Hartmann, 1984; Kaynia and Kausel, 1991; Sadek and Shahrour, 2004). Subsequent developments over the past two decades have mainly addressed the expansion of the coupling domain (Γ_c) from an interaction line (Engin et al., 2007; Tschuchnigg, 2013; Ninić et al., 2014) to an interaction surface (Turello et al., 2016; Ghofrani, 2018; Truty, 2023). Related formulations are referred to as embedded FE model with implicit interaction line (EB-L) and implicit interaction surface (EB-I), respectively (Granitzer et al., 2024d). Compared to the dimensionally reduced description of the soil-structure interaction behavior along the centerline pursued by EB-Ls, EB-Is render fully surface-to-surface contact problems, that is, coupling between Ω^p and Ω^s is numerically realized over the physical soil-pile contact geometry. In preceding contributions of the authors (Granitzer and Tschuchnigg, 2021; Granitzer and Tschuchnigg, 2023), relative merits of this feature have been highlighted based on comparative studies employing the EB-I formulation proposed by Granitzer et al. (2024d), currently implemented in a research kernel of the FE code PLAXIS 3D (Bentley Systems, 2023). These include, but are not restricted to, the reduced mesh size sensitivity, suppression of numerical oscillations in the skin traction profile, improved conditioning of the tangent stiffness matrix, more genuine transfer of external loads and ability to analyze normal stresses at the soil-pile contact. However, the reader should notice that this numerical evidence has been mainly obtained based on single pile analyses. While this problem class is useful for the appraisal of novel embedded FE models (Turello et al., 2016), single pile studies provide limited insight into their suitability for the analysis of large-scale foundation systems, that are typically characterized by complex pile-ground-structure interaction phenomena (Hanisch et al., 2002) and eccentric loading conditions (Franza and Sheil, 2021; Bhartiya et al., 2024). This distinct lack of research is additionally highlighted in a recent publication (Granitzer et al., 2024c) and manifests in the pending rollout of the developed EB-I model in the commercial version of the FE code PLAXIS 3D. In this light, the present paper, on the one hand, aims to investigate the applicability of the developed EB-I for the analysis of practically relevant BVPs involving multiple piles. On the other hand, it provides practice-oriented insight into the relevance of selected EB-I parameters. For this purpose, three different pile foundation systems are analyzed. The credibility of the EB-I predictions is assessed based on comparisons with both, the numerical SFEA benchmark and *in situ* measurements.

The remainder of this manuscript is organized as follows: Section 2 concisely recapitulates the relevant theoretical background and visualizes the principal components of the EB-I model introduced by Granitzer et al. (2024d). As a main scientific contribution of this work, sections 3–5 analyze the performance of this formulation considering three different pile foundation systems with varying pile arrangements and loading conditions. These include (i) an idealized 3 × 3 capped pile group subjected to an eccentric vertical load, (ii) a pile-supported integral bridge pier experiencing combined vertical and horizontal loading and (iii) a

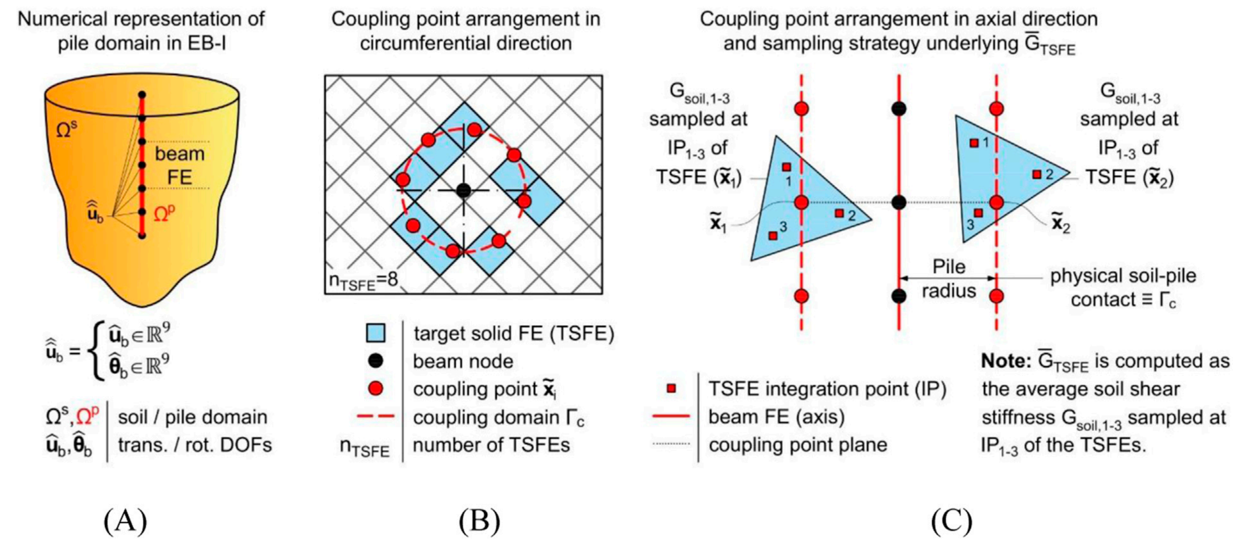

FIGURE 1
(A) Schematic of pile-soil coupling problem discretized by means of embedded FE model with implicit interaction surface, along with coupling point distribution in **(B)** circumferential direction of distinct coupling point plane and **(C)** axial direction, including coupling point embeddings in two different target solid FEs. For clarity, coupling point arrangements are shown for a simplified 2D mesh.

piled raft foundation with non-symmetric geometry founded on multi-layered ground with inclined soil layer boundaries. Section 6 closes with the conclusions of this work.

2 Background

To render this paper self-contained, this section addresses relevant aspects of the EB-I formulation validated in this work. Full details can be found in Granitzer et al. (2024a), Granitzer et al. (2024c), Granitzer et al. (2024d).

2.1 Embedded beam with implicit interaction surface

Figure 1 illustrates the principal framework of the EB-I proposed by the authors. Ω^p is discretized by means of 3-noded shear flexible Timoshenko beam FEs with three rotational ($\hat{\theta}_b$) and translation ($\hat{u}_b$) DOFs per node; see Figure 1A. Coupling between Ω^p and Ω^s is locally described at coupling point ($\tilde{x}_i$) level employing a point collation method (Ghofrani, 2018). Therefore, equilibrium between Ω^p and Ω^s is locally satisfied at multiple $\tilde{x}_i$, which are placed at regular intervals in axial and circumferential direction across Γ_c; compare Figure 1B, where the circumferential arrangement of $\tilde{x}_i$ is shown for one distinct coupling point plane.

From a mechanical perspective, the EB-I induces a point-wise traction system over Γ_c, defined on the basis of elasto-plastic relationships. Employing the displacement coupling method (Steinbrecher et al., 2022a), this involves tracking the relative displacement vector $\tilde{u}_{rel} = \tilde{u}_b - \tilde{u}_s$ between Ω^p and Ω^s at all $\tilde{x}_i$. On the beam side, this requires the formulation of a mapping scheme that converts the nodal DOFs of multiple 3-noded beam FEs, $\hat{\boldsymbol{u}}_b \in \mathbb{R}^{18}$, defined along the beam centerline, into the discrete beam displacement vector $\tilde{\boldsymbol{u}}_b \in \mathbb{R}^3$ at the physical soil-pile contact, expressed by:

$$\tilde{\boldsymbol{u}}_b\left(\tilde{\boldsymbol{x}}_i\right) = \boldsymbol{H} \cdot \hat{\boldsymbol{u}}_b \tag{1}$$

In Equation 1, $\boldsymbol{H} \in \mathbb{R}^{3x18}$ denotes the mapping function matrix. On the solid side, $\tilde{\boldsymbol{u}}_s \in \mathbb{R}^3$ is interpolated within the respective target solid FE (TSFE) that encloses $\tilde{\boldsymbol{x}}_i$; compare Figure 1A. From Figure 1B, C, it can be inferred that the TSFE varies for the majority of $\tilde{\boldsymbol{x}}_i$. In this context, the interested reader may refer to Granitzer et al. (2024c) for details concerning the global search algorithm employed to identify related $\tilde{\boldsymbol{x}}_i$-TSFE pairs. On this basis, the embedded interface constitutive relationship of the discrete traction vector $\tilde{\boldsymbol{t}}$ system under stick conditions can be written in compact form as:

$$\tilde{\boldsymbol{t}} = \boldsymbol{K} \cdot \tilde{\boldsymbol{u}}_{rel}, \forall\, \tilde{\boldsymbol{x}}_i \in \Gamma_c \tag{2}$$

where the embedded interface stiffness matrix $\boldsymbol{K} = f\left(R_{pile}, \nu_i, \bar{G}_{TSFE}, \Gamma_s, \Gamma_b\right)$ is defined as a function of the pile radius R_{pile}, interface Poisson's ratio ν_i, mean of the current soil shear stiffness (G_{soil}) sampled at the TSFE integration points ($\bar{G}_{TSFE}$; cf. Figure 1C) and embedded interface stiffness multipliers Γ_s, Γ_b belonging to the set of $\tilde{\boldsymbol{x}}_i$ located at the shaft and the base of Γ_c, respectively.

In Equation 2, $\bar{G}_{TSFE}$ allows to account for both, the influence of the *in situ* state of stress in the soil surrounding the EB-I and the relative stiffness between Ω^p and Ω^s on the load transfer along the pile shaft (Stewart and Kulhawy, 1981; Rajapakse, 1990). Provided that the stress dependency of G_{soil} is considered in the FEA (for example, by using the Hardening Soil Small model after Benz et al., 2009), Tschuchnigg and Schweiger (2015) conclude that this feature is essential to realistically capture the mobilization of skin resistance of an EB-L formulation. This observation has been confirmed by Granitzer et al. (2024d) with respect to the EB-I, indicating that the rationale underlying $\bar{G}_{TSFE}$ can be seamlessly transferred to different embedded FE models and is not specific to a certain solid FE type.

2.2 Calibration of interface constitutive model parameters

With regard to the embedded interface constitutive relationship described in Equation 2, it should be pointed out that Γ_s, Γ_b represent calibration parameters that influence both, the pile load-displacement response as well as the load sharing between the EB-I shaft and base, respectively. This extension increases the flexibility in the use of EB-Is, as these parameters can be modified to refine numerical predictions on a site-specific scale (e.g., based on load-settlement curves obtained from static pile load tests or numerical benchmark models). While favorable effects of an adequate parameter value selection on the fidelity of EB-I predictions have been reported in a number of studies (Smulders et al., 2019; Granitzer and Tschuchnigg, 2023), there has been little guidance in the literature on the underlying calibration procedure.

This lack of reliable methods to determine Γ_s, Γ_b has motivated the development of an automatic calibration framework (ACF) based on box-constrained Particle Swarm Optimization (Helwig, 2010), with the aim to simplify the parameter calibration procedure and exploit available benchmark data sources; see Granitzer et al. (2024a). Conceptually, the proposed ACF renders this calibration task as an optimization problem, similar to the selection of the initial spring stiffness in traditional t-z and p-y type models; see He and Kaynia (2024); Sheil and McCabe (2016). The basic idea is to calibrate the parameter vector $\boldsymbol{x} = [\Gamma_s, \Gamma_b]^T$, such that the load-displacement curve obtained with the EB-I is as close as possible to the provided benchmark data, for instance, in the form of *in situ* measurements, practical experience documented in the pertinent literature (DGGT, 2014), numerical benchmark simulations (Turello et al., 2016) or closed-form solutions (Randolph and Wroth, 1979). For this purpose, a global optimizer is implemented that operates in parallel on a set of $\boldsymbol{x}$ and iteratively adjusts the parameter values until a good fit is obtained. To date, the applicability of the ACF for the determination of Γ_s, Γ_b has been demonstrated based on three different pile problems under axial vertical loading considering uniform and multi-layer soil conditions (Granitzer et al., 2024a). In Section 3, the validation scope will be supplemented by detailed analyses of a capped pile group with pronounced load eccentricity.

2.3 Normal stress recovery methods

To identify the onset of pile-soil slippage, the embedded interface constitutive model formulated within the framework of elastoplasticity employs a Coulomb-type frictional slip criterion, written as:

$$\sqrt{\tilde{t}_2^{\,2} + \tilde{t}_3^{\,2}} \leq \left(c' + \tilde{\sigma}_n^{'} \tan\varphi'\right) \cdot R_{inter}, \forall\, \tilde{\boldsymbol{x}}_i \in \Gamma_c \tag{3}$$

In Equation 3, $\tilde{t}_2$, $\tilde{t}_3$ are the traction vector components in both tangential directions, c' and φ' are the effective shear strength parameters of the TSFE, $\tilde{\sigma}_n^{'}$ represents the effective normal stress and R_{inter} denotes the interface shear strength reduction factor. Due to the implicit nature of their Γ_c, embedded FE models with frictional contact generally require the recovery of $\tilde{\sigma}_n^{'}$ at multiple $\tilde{\boldsymbol{x}}_i$ that, in turn, occupy arbitrary positions inside the solid mesh. Contrary to piles modeled by means of the SFEA, where $\tilde{\sigma}_n^{'}$ can be directly sampled at the integration points of explicit interface FEs (Day and Potts, 1994; Staubach et al., 2022), this characteristic renders the determination of $\tilde{\sigma}_n^{'}$ dependent on a normal stress recovery technique (NRC). In this context, Granitzer et al. (2024c) have proposed three different strategies implemented within the EB-I framework, namely, the penalty, local and non-local NRC. As visually explained in Figure 2 for one distinct $\tilde{\boldsymbol{x}}_i$, they differ in terms of the stress calculation domain, that is, the set of coupling variables used to recover $\tilde{\sigma}_n^{'}$. In the penalty approach, normal stress changes are directly related to the relative displacement increments between the nodes of the beam FE and the solid FE that encloses $\tilde{\boldsymbol{x}}_i$, referred to as local TSFE. In contrast, the local and non-local NRCs recover $\tilde{\sigma}_n^{'}$ from the actual stress state of the surrounding soil. Therefore, the solid stress tensors sampled at the integration points of the local and non-local TSFEs, respectively, have to be projected onto $\tilde{\boldsymbol{x}}_i$. The salient difference between the local and non-local NRC concerns the stress calculation domain, whereas the latter additionally involves the integration points of the non-local TSFEs; see Figure 2.

Non-local strategies have also found application in the form of strain regularization schemes of strain-softening soil constitutive models, with the aim to compromise the mesh dependency resulting from localized concentrations in the computed field variables (Galavi and Schweiger, 2010; Cui et al., 2023). With reference to the EB-I, a conceptually similar obstacle arises due to the mobilization of multiple discrete traction vectors localized at $\tilde{\boldsymbol{x}}_i$ (Steinbrecher et al., 2020). Nevertheless, Granitzer et al. (2024c) report a comparable performance of the three different NRCs, that is, also in the case of an expanded stress calculation domain, as considered in the non-local NRC. It should be pointed out that this numerical evidence has been constrained to single pile analyses to date. Therefore, it remains unclear whether this observation scales to large-scale BVPs as well. For this purpose, Section 5 examines the performance of the three NRCs based on a piled raft case study.

3 Capped pile group

This section employs a 3 x 3 capped pile group to assess the applicability of the EB-I for cases with notable pile-soil-pile interaction effects and eccentrical vertical loads. Subsection 3.1 describes the analyzed reference scenario, followed by the calibration of interface constitutive model parameters in Subsection 3.2. Subsection 3.3 numerically validates the EB-I against the numerical SFEA benchmark.

3.1 Investigated scenario and model description

The analysis domain dimensions and boundary conditions are adopted from Franza and Sheil (2021). In their work, this reference scenario is used to validate an EB-L formulation under multi-directional loading, notably without providing details about the

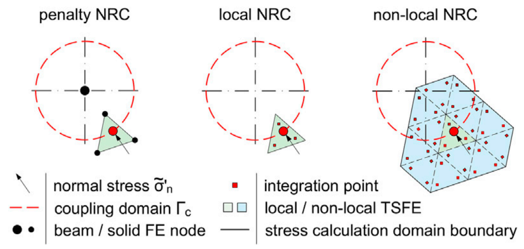

FIGURE 2
Schematic of normal stress recovery techniques after Granitzer et al. (2024c) described for one EB-I coupling point. For clarity, the stress calculation domains and corresponding coupling variables are shown for a simplified 2D mesh.

NRC and calibration of interface constitutive model parameters; cf. Section 2.2 to Section 2.3. Figure 3 shows the foundation geometry that consists of an elevated cap underpinned by a 3 x 3 pile group, with a spacing of $5 \cdot D_{pile}$ between the pile centers.

The rigid cap is modeled as a weightless plate FE and rigidly attached to the piles. It is noticed that the cap is not in contact with the underlying soil. Therefore, the foundation behavior is fully controlled by the pile-soil-pile interaction, which renders this geometrical configuration particularly suitable for EB-I validation purposes. All piles are assumed elastic ($E_{pile} = 30\ GPa, \nu_{pile} = 0.2$) and have an embedment length $L = 12.5\,m$, pile diameter $D_{pile} = 0.5\,m$, unit weight $\gamma_{pile} = 25\,kN/m^3$ and interface shear strength reduction factor $R_{inter} = 0.9$. In analogy to the EB-I configuration employed in Granitzer et al. (2024d), the EB-I piles are assigned with the local NRC to limit the skin friction and 8 circumferential $\tilde{\boldsymbol{x}}_i$ per coupling point plane, similar to Figure 1B. The embedded interface stiffness multipliers Γ_s, Γ_b are calibrated employing the ACF, as will be demonstrated in Section 3.2.

In all simulations, the SFEA serves as a benchmark model for numerical validation (Jauregui and Silva, 2011); compare Section 1. Therefore, an additional FE model is generated where the piles are explicitly discretized by means of solid FEs (i.e., representing Ω^p) and zero-thickness interface FEs (Day and Potts, 1994) to realistically capture soil-structure interaction effects. To ensure that boundary effects are reduced to an acceptable limit, the model dimensions and SFEA mesh topology shown in Figure 3 are defined based on preliminary studies, similar to the trial simulations presented in Granitzer and Tschuchnigg (2021). From the displayed mesh topologies, it can be inferred that the quadratic tetrahedral solid FE number could be substantially reduced from 218,163 to 29,886 using the EB-I instead of the SFEA for the pile modeling.

The Hardening Soil Small (HSS) soil constitutive parameters (Benz et al., 2009) representing Vienna fine sand are adopted from Tschuchnigg and Schweiger (2010). For simplicity, the influence of groundwater is neglected. The step simulation sequence comprises three principal steps: (i) generation of the initial stress field, (ii) activation of Ω^p and (iii) displacement-driven foundation loading. To analyze eccentric actions, a monotonic point load F_z with displacement magnitude $u_z = 0.1 \cdot D_{pile}$ and a varying eccentricity in x-direction is applied at (e, 0, 0) to the cap; see Figure 3.

3.2 Calibration of interface constitutive model parameters

With reference to Section 3.2, Γ_s, Γ_b are calibrated employing the ACF presented in Granitzer et al. (2024a), combined with the PSO search space constraints and hyperparameters proposed by the authors. Following the recommendations given in this work, the calibration is carried out considering a geometrically reduced representation of the capped pile group geometry (that is, only the center pile is activated during the loading phase, instead of the full 3 x 3 pile group) to improve the runtime efficiency of the calibration procedure.

Figure 4A provides insight into the convergence behavior of the automatic calibration, in the form of the relative squared error (E_{RSE}), which indicates the quality of the best, worst and mean EB-I candidate solution for $\boldsymbol{x} = [\Gamma_s, \Gamma_b]^T$ found within each iteration. The results show reasonable convergence rates, which is substantiated by a E_{RSE}-reduction of more than one magnitude of order in the mean error. Figure 4B visualizes the corresponding density contours of the 400 candidate solutions observed during the calibration procedure. As could be expected, the optimal parameter vector $\boldsymbol{x}_{opt} = [\Gamma_s = 0.010, \Gamma_b = 0.012]^T$ is identified in the vicinity of the high-density area. In this context, the reader should notice that $\boldsymbol{x}_{opt}$ refers to the E_{RSE}-value of the best candidate solution found after 20 iterations. In the next subsection, this parameter set is consequently adopted to investigate the applicability of the EB-I for the analysis of the capped pile foundation.

As a key outcome of the calibration procedure, Figure 5 illustrates the EB-I load-settlement curve obtained with $\boldsymbol{x}_{opt}$. From the results, it becomes obvious that the EB-I with calibrated values for Γ_s, Γ_b achieves an exceptional agreement with the numerical SFEA benchmark. A comparison of the calibrated EB-I response with the gray-shaded area, constituting the bandwidth of all 400 candidate solutions observed during the calibration, further underlines that the parameter value selection with respect to Γ_s, Γ_b considerably governs the numerical fidelity of the EB-I. This observation aligns with the results of related studies presented in Granitzer et al. (2024a). In should be pointed out that the underlying calibration task could be effectively solved with minimum user effort employing the ACF.

3.3 Parametric study

The first set of analyses investigates the effect of eccentric vertical loads on the roto-translational behavior of the capped pile group. Figure 6 displays the normalized settlement (u_z/D_{pile}) and rotation around the y-axis (θ_y). In analogy to Franza and Sheil (2021), the results are evaluated at the intersection of the central pile with the soil subsurface level. While the load eccentricity has an insignificant influence on the initial pile response, it decreases the pile resistance at large settlements. Correspondingly, the load eccentricity significantly influences the development θ_y over the full load range, whereas θ_y-values increase with increasing normalized eccentricity (e/D_{pile}). This tendency can be attributed to the mobilization of lateral soil resistance induced by the external

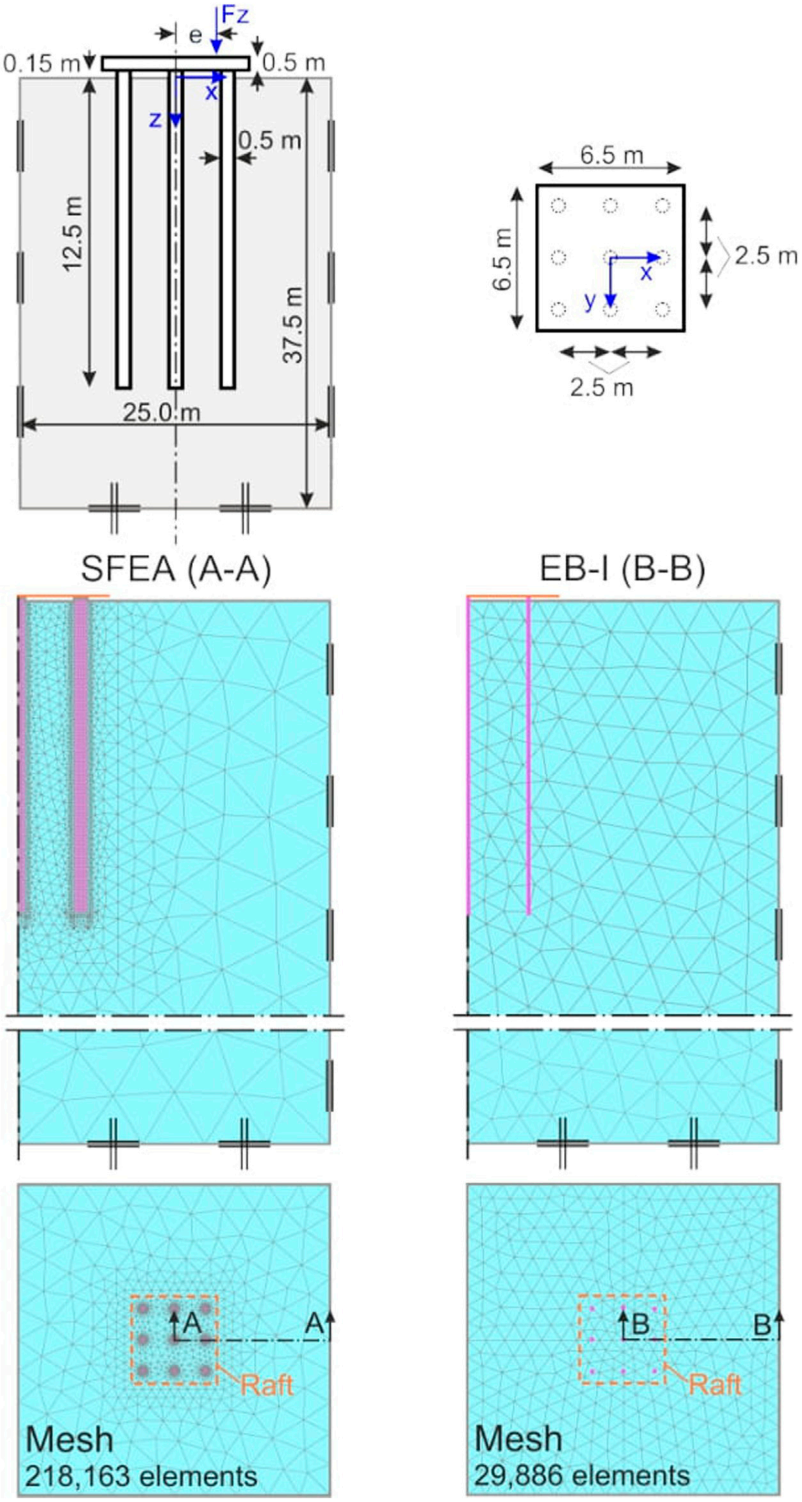

FIGURE 3
Geometry and load configuration of capped pile group adopted from Franza and Sheil (2021), along with mesh topologies of standard FE approach (SFEA) and EB-I model, respectively.

bending moment, which increases with increasing load eccentricity. In this light, non-zero load eccentricities are equivalent to the application of an additional horizontal load component at the center of the pile cap (Franza and Sheil, 2021). Consequently, the load eccentricity has an impact on both, the vertical capacity and the failure mode of the pile group, which generally changes from axial pile failure to rather complex failure mechanisms that are also controlled by the lateral soil strength. The validity of the

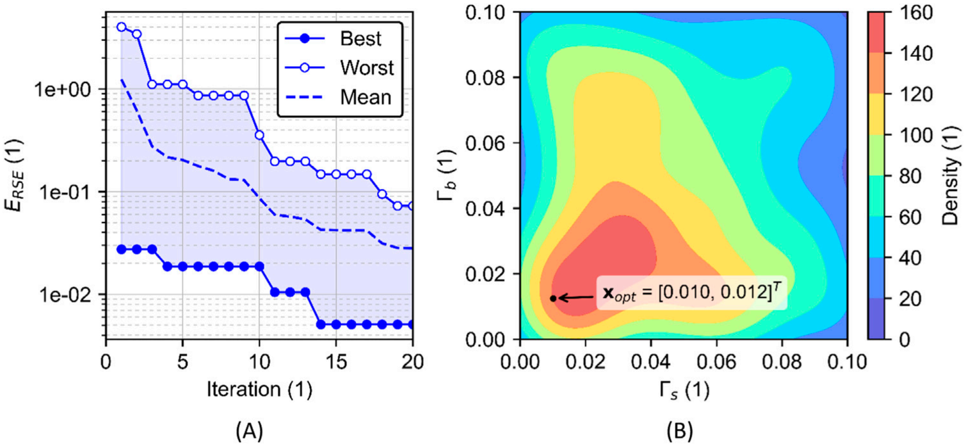

FIGURE 4
Visualization of **(A)** the convergence behavior, described as a reduction in the relative squared error ($\mathbf{E}_{\mathrm{RSE}}$) over the iteration cycles, along with **(B)** the density contour plot showing the distribution of the 400 candidate solutions observed during the automatic calibration.

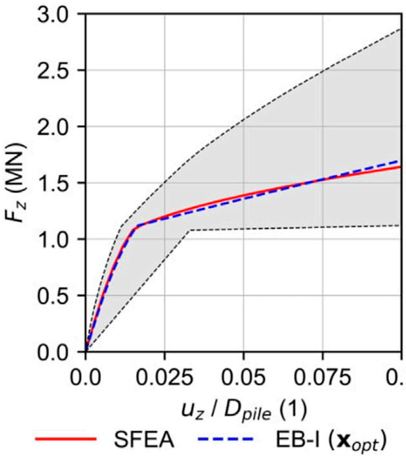

FIGURE 5
Comparison of load-settlement curves obtained with numerical SFEA benchmark and calibrated EB-I with optimal parameter vector ($\mathbf{x}_{\mathrm{opt}}$). The gray-shaded area shows the range of EB-I results observed during the automatic calibration procedure.

simulation results is qualitatively confirmed by small-scale tests on pile groups resting on sand (Kishida and Meyerhof, 1966; Meyerhof et al., 1983) and interaction diagrams based on limit analysis theorems (Di Laora et al., 2019).

Figure 7 provides additional insight into the pile model predictions evaluated at the pile head positions. Due to symmetry conditions about the mid-plane (y = 0 m), corresponding piles placed along the upper and lower row of the foundation, respectively, show an identical load-displacement behavior. An interesting detail can be observed for the piles located along the left row of the pile group, where the roto-translational behavior of the pile group leads to pile uplift for $e/D_{pile} = 5$. Essentially, EB-I results show overall a very good agreement with the numerical SFEA benchmark, despite the relatively coarser mesh topology employed in the EB-I simulations. This numerical evidence for the first time demonstrates the suitability of the EB-I for the analysis of pile foundations under eccentric vertical loads.

4 Pile-supported pier of integral railway bridge

The next section employs an integral bridge case study to examine the EB-I performance under combined vertical and horizontal loading. In addition, it provides guidance in the unit weight selection of EB-Is, an ambiguous material parameter due to the inherent overlapping of the subdomains (that is, Ω^p and Ω^s) in embedded FE models. Section 4.1 concisely describes the investigated scenario, followed by FE model details and back-analyses presented in Section 4.2 and Section 4.3.

4.1 Case study: integral railway bridge Ems-Jade-Channel

As part of the restructuring of the double-track railway line extending between Oldenburg and Wilhelmshaven in Germany, a new 83-meter-long railway bridge has been constructed over the Ems-Jade canal near Sande. The latter has been designed as three-span composite steel integral bridge, without joints and bearings (see Figure 8), and has been in service since 2021.

Before the bridge construction, a comprehensive program of field and laboratory testing has been carried out to evaluate the subsoil conditions (DB ProjektBau GmbH, 2013). Moreover, vertical and horizontal static pile load tests have been conducted to assess the load-displacement behavior of the pier foundation piles and deduce foundation stiffness parameters for the structural model (DB E and C, 2019). The bridge is founded on soft soil deposits with high compressibility and low permeability, comprising a variable mixture of peat, clay, silt and sand to a depth of around 11 m below the ground subsurface. The soft soil alternations are underlain by the load-bearing stratum comprising medium to dense sand. The (partly

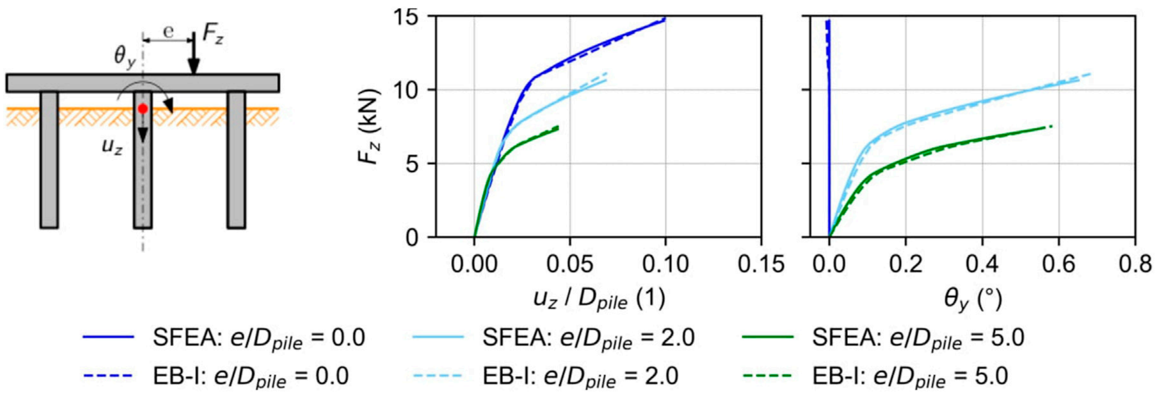

FIGURE 6
Global response of capped pile group as function of normalized vertical load eccentricity and pile modeling approach.

confined) groundwater table is observed close to the ground surface. To avoid excessive long-term settlements of the railway embankments adjacent to the bridge abutments and to speed up the consolidation process, preloading measures combined with vertical drains have been implemented over a period of several months before the bridge construction. As an additional measure to reduce the settlements to an acceptable limit and ensure the serviceability of the bridge under operating conditions, vertical loads originating from the superstructure and the piers are transferred via large-diameter bored pile groups ($D_{pile} = 1.2\,m$) into the load-bearing stratum; see Figure 8B. These pile groups beneath both piers at axis 10 and 20 consist of 18 piles, 12 of which have an inclination of 1:6 to resist horizontal loads in longitudinal bridge direction resulting from train driving and braking.

Owing to the rigid connection between the superstructure and the substructure (including abutments, piers and foundations), integral bridges are typically characterized by seasonal lateral deformations induced by the longitudinal thermal expansion of the superstructure (Stastny et al., 2022; Stastny et al., 2024). To this date, however, experimental evidence of thermo-mechanical effects on the structural behavior of integral bridges is rare. To some some extent, this distinct lack of knowledge has motivated the installation of an extensive long-term monitoring system (MKP, 2020). In this respect, Figure 8B provides insight into the monitoring equipment at axis 20. A visual description of the full instrumentation, which has begun operation in November 2021, can be found in Granitzer et al. (2024b). In addition to the recordings related to the composite superstructure, the monitoring focuses on the structural behavior of the substructure components. Essentially, this involves horizontal displacement measurements of (i) selected foundation piles, recorded by means of 14-m-long chain inclinometers, and (ii) relative displacement measurements between the bridge piers at axis 10 and 20 via laser distance measurement (Figure 8B). Subsequently, these results form the basis of the numerical back-analysis and EB-I validation studies.

4.2 Finite element model description

The EB-I is validated by employing a geometrically reduced detail of the integral bridge at axis 20; see Figure 8B. As can be inferred from Figure 9, this includes the pier and the pile foundation system. Numerical back-analyses are conducted considering a quasi-static representation of the horizontal temperature loads related to the expansion of the bridge superstructure. A comparison with both, measurement results and the numerical SFEA benchmark model, for the first time provides insight into the EB-I performance under combined vertical and horizontal loading.

The soil layering, along with the calibrated Soft Soil (Bentley Systems, 2023) and HSS parameters to describe the soil constitutive behavior of the soft soil alterations and sand layer, respectively, are defined based on the real project data. The calibrated soil constitutive parameter sets have been found suitable for the numerical back-analyses of static pile load tests (DB E and C, 2019). Figure 9 shows the model dimensions and SFEA mesh topology (comprising 346,875 quadratic tetrahedral solid FEs), which are selected based on domain and mesh sensitivity analyses; compare Granitzer and Tschuchnigg (2021). As discussed in Section 1, high mesh refinements around the piles could be circumvented by using EB-Is for the pile modeling, leading to a significantly reduced number of 176,818 solid FEs. Regardless of the pile modeling approach, the piles are assumed elastic ($E_{pile} = 32.7\ GPa, \nu_{pile} = 0.2$) and assigned with $R_{inter} = 0.9$ at the soil-pile contacts. To ensure a rigid connection at the pile-raft connection, EB-I piles are modeled "perforated", that is, the pile heads are embedded into the slab up to half of the slab height; see Figure 9. The groundwater table is set at the ground surface level. To adequately address the partially confined groundwater conditions in the project area, preliminary FEA focusing on the pile behavior under drained and undrained soil conditions have been performed. The results (not shown) indicate a subordinate influence of the drainage conditions on the pile response, which is attributed to the dominant load transfer of the foundation loads into the drained load-bearing stratum. Therefore, drained soil conditions are regarded as adequate for the main study.

All simulations are conducted utilizing the identical calculation phase sequence. In the initial phase, the initial stress field is generated using the so-called K0 procedure (Bentley Systems, 2023). In this calculation phase, only soil clusters are active and gravity loads are

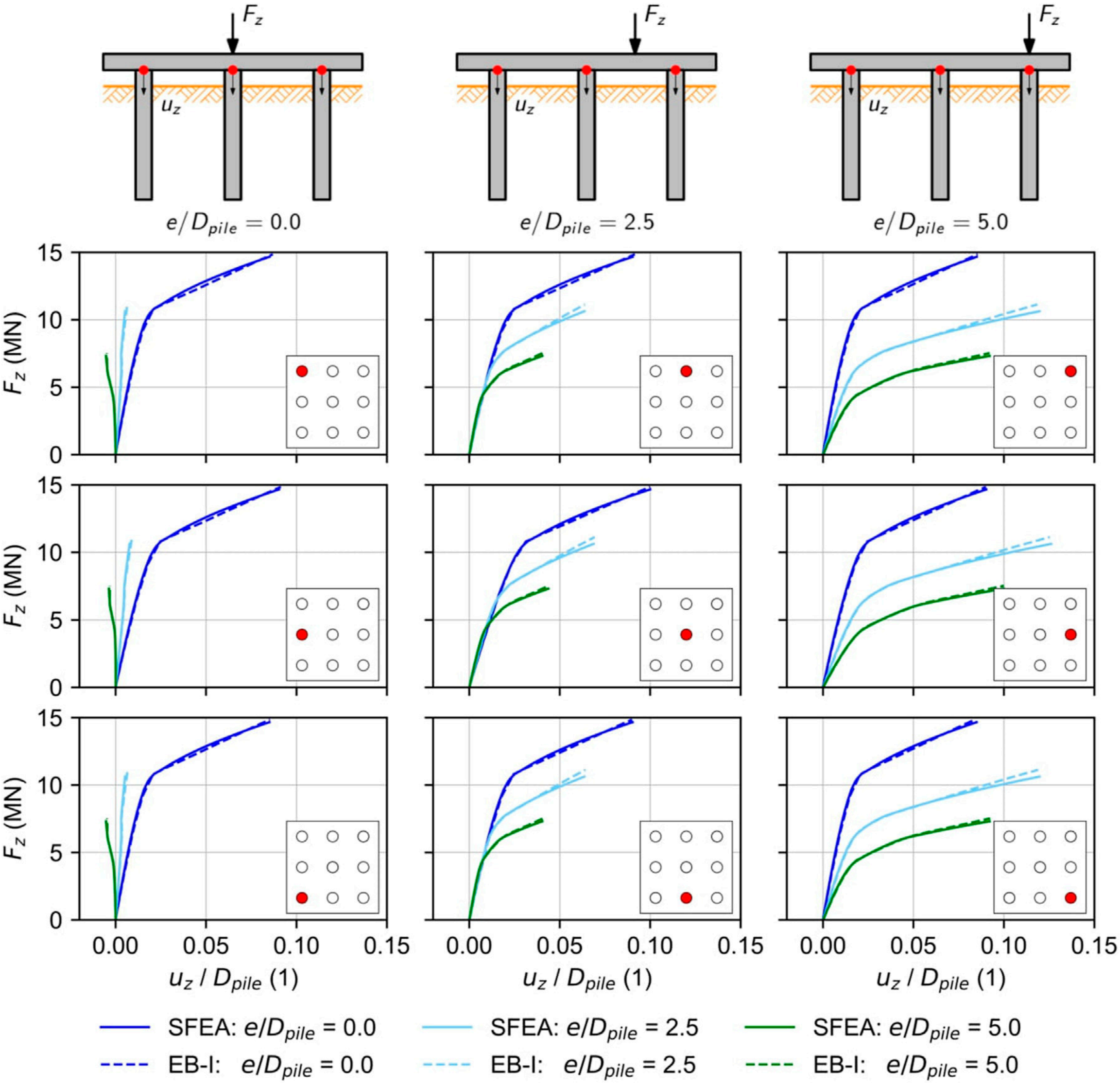

FIGURE 7
Load-displacement curves as function of the normalized vertical load eccentricity, pile modeling approach and pile position.

applied. The latter are derived from the soil unit weight and balanced by the effective vertical soil stresses. Next, the piles are wished in place, followed by an activation of the slab and the pier. Subsequently, stage construction effects are considered in the form of Neumann boundary conditions imposed at the top surface of the pier; see Figure 9. The corresponding distributed vertical loads comprise (i) permanent ($g = 265\ kPa$) loads from the superstructure and (ii) traffic loads ($q = 222\ kPa$) associated with the two railway tracks, which are determined according to the LM71 railway bridge loading diagram (CEN, 2003). Since the traffic loads represent a transient loading component, they are deactivated in the penultimate calculation phase. In this way, traffic-induced stage construction effects on the "permanent" soil displacements are, to some extent, constrained. The final simulation phase concerns the quasi-static representation of thermo-mechanical effects induced by the expansion of the superstructure within the first summer cycle (S0: 01/2022 – S1: 07/2022); compare Figure 10A. For this purpose, Dirichlet boundary conditions in the form of uniformly distributed horizontal surface displacements are imposed over a height of 2.2 m across the crossbeam area; see Figure 9. The horizontal displacement magnitude Δu_x applied in this simulation phase is approximated based on horizontal laser distance measurements u_x between the piers at axis 10 and 20; see Figure 10A. Adopting symmetry conditions, the relative displacement rest point between the piers is assumed at the center of the bridge span between axis 10 and axis 20, hence $\Delta u_x = 6.2 / 2 = 3.1\,mm$ is applied in the simulations.

4.3 Back-analysis and parametric study

Although the pile unit weight has a relatively low parameter uncertainty (Mendez et al., 2021) in the FEA of geotechnical problems, the implementational framework of overlay domain decomposition methods (Cai, 2003), such as embedded FE

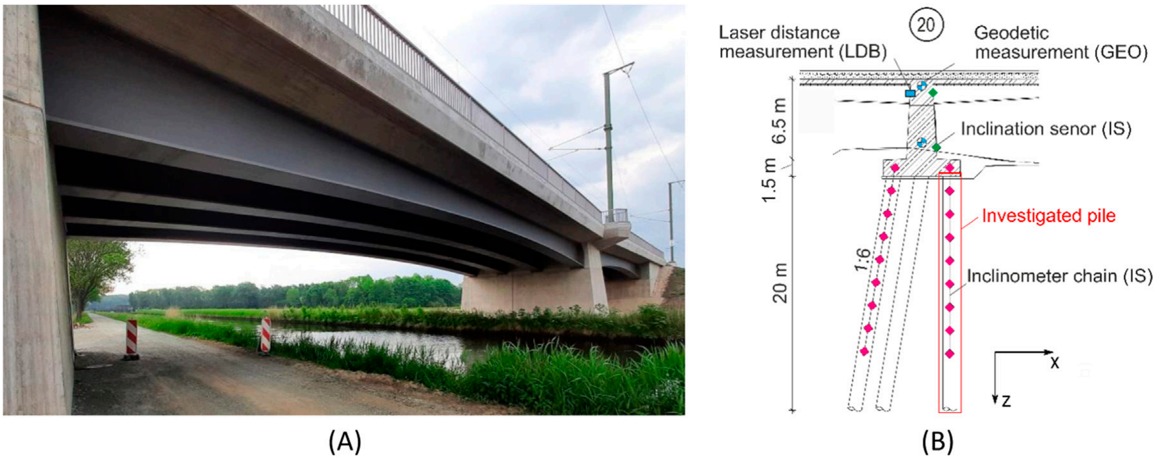

FIGURE 8
(A) Composite steel integral bridge (Oldenburg – Wilhelmshaven) span between axis 10 and 20 (MKP, 2020); **(B)** detailed view of the pier monitoring equipment at axis 20.

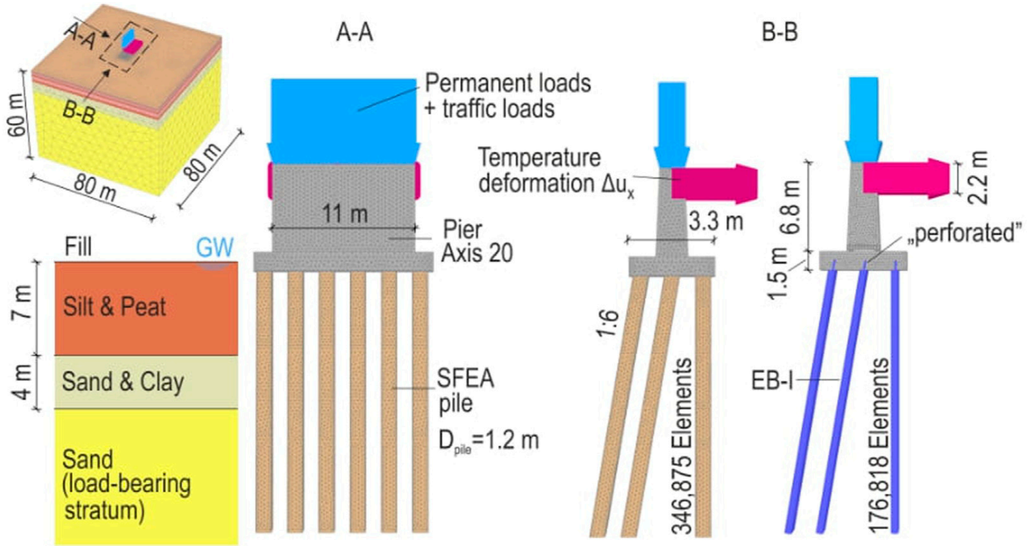

FIGURE 9
Visual representation of back-analysis domain and boundary conditions for analyzed integral bridge detail at axis 20, along with mesh topology. To provide insight into the SFEA pile discretization, zero-thickness interface elements are not shown.

models, renders the underlying parameter selection non-trivial. This rationale is supported by the different approaches reported in the literature, where this parameter is either not documented (Tschuchnigg and Schweiger, 2010; Oliveria and Wong, 2011), defined according to the physical pile unit weight (Tradigo et al., 2016) or assigned with the delta unit weight (Lődör and Balázs, 2018; Watcharasawe et al., 2021), representing the delta unit weight of the pile to the surrounding soil ($\gamma_{pile} - \gamma_{soil}$). This observed inconsistency can be attributed to the dimensionally reduced representation of Ω^p in embedded FE models as line geometry and its superposition onto Ω^s (that is, the EB-I does not exclusively occupy the physical pile volume); compare Section 1. It may therefore be argued that a reduction in the unit weight of embedded FE models is reasonable to ensure mass balance of the overlapping domains (Tschuchnigg and Schweiger, 2015) and to adequately address global interaction phenomena between piles and surrounding structures in the analysis domain (Williamson et al., 2017; Franza and Marshall, 2019). However, this modeling strategy leads to layer-dependent parameter values in cases where piles are embedded in multi-layered ground with varying γ_{soil}. Moreover, it should be pointed out that a reduced pile unit weight may significantly underestimate the "residual loads" (that is, loads which are

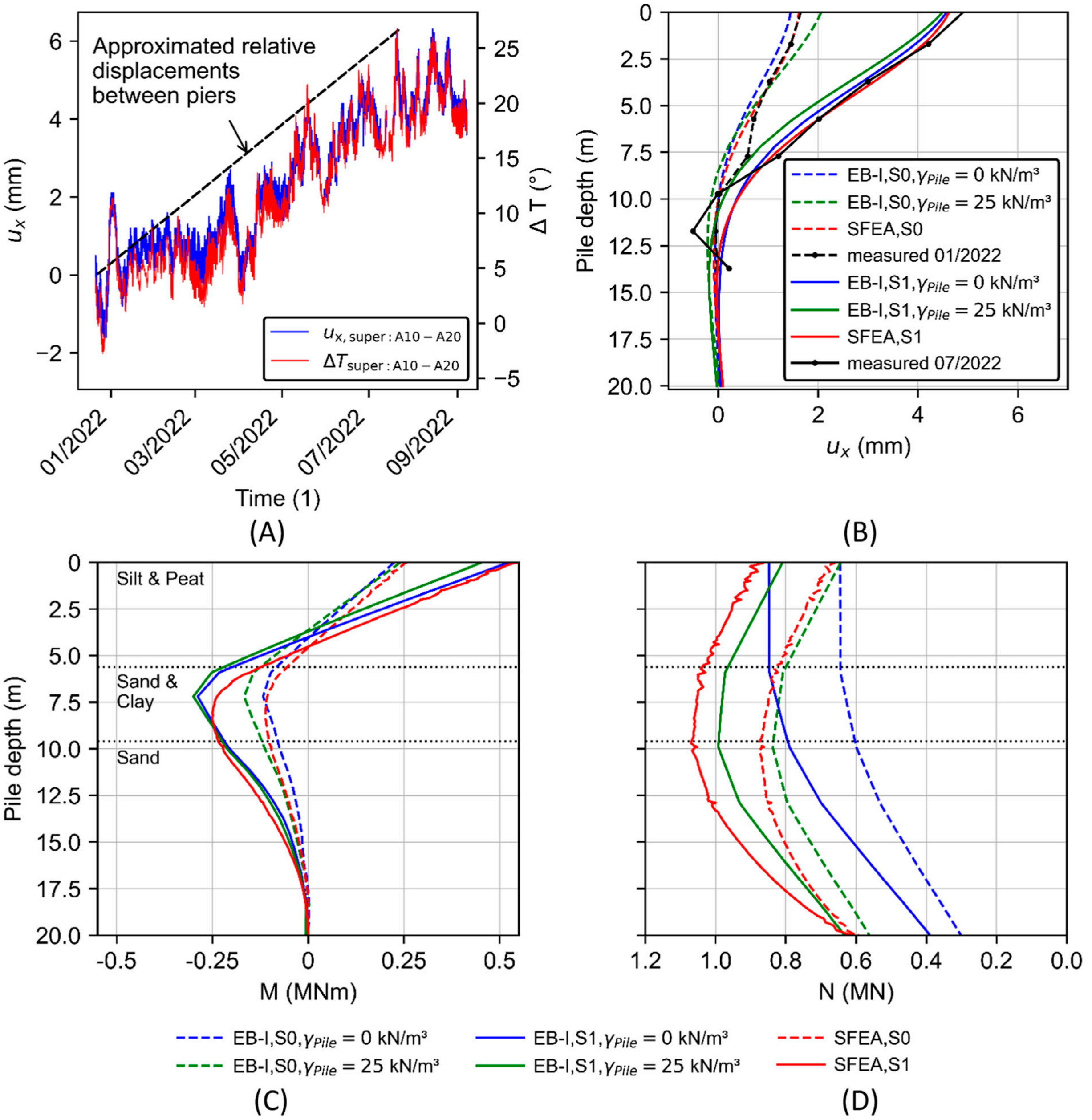

FIGURE 10
(A) Evolution of horizontal relative displacements $\mathbf{u_x}$ between piers, along with strain-effective temperature Δ**T** of superstructure; **(B)** comparison of measured and back-calculated horizontal pile displacements after final phase at start (S0) and end (S1) of first summer cycle. Influence of pile modeling approach and unit weight on **(C)** bending moment and **(D)** normal force distribution.

always present in the pile, even before measurements are taken or analyses performed), potentially resulting in unsafe designs (Fellenius and Altaee, 1995).

To study the relative importance of the selected EB-I unit weight on the credibility of pile predictions, the instrumented pile (Figure 8B) is back-calculated deploying $\gamma_{pile} = 0\,kN/m^3$ and $\gamma_{pile} = 25\,kN/m^3$ for the EB-Is. A comparison of the simulation results with the horizontal pile displacement profiles measured at the start (S0) and the end (S1) of the first summer cycle reveals three interesting details; see Figure 10A. First, notable horizontal pile displacements are observed immediately after the completion of the superstructure, which can be attributed to the asymmetrical geometry of the pier foundation; see Figure 9. Next, the results infer that the majority of horizontal pile displacements occurs within the soft soil layers, which provide relatively low lateral support (DGGT, 2014) down to a pile depth of 10 m; compare Figure 9. In contrast, thermo-mechanical effects of the superstructure have a negligible influence on the horizontal pile displacements evolving along the load-bearing sand stratum. At final, it can be observed that all pile models capture the pile measurements with high accuracy, regardless of the pile modeling approach and selected unit weight. The same applies for the bending moment distributions shown in Figure 10C for the EB-I models and numerical SFEA benchmark, which show comparable results.

While the EB-I unit weight has a subordinate importance on the horizontal pile displacements and bending moments, Figure 10D demonstrates that this parameter significantly affects the computed normal force distribution. Apparently, relative differences between the analyzed EB-I configurations increase with increasing pile depth. This observed tendency is not surprising as it can be explained by the influence of the underlying "residual loads" on the pile normal force; cf. Fellenius and Altaee (1995). Essentially, the use of EB-Is with zero-valued pile unit weight considerably underestimates the numerical SFEA benchmark results, whereas it shows reasonable agreement for $\gamma_{pile} = 25\,kN/m^3$. From an engineering point of view, the above discussion pinpoints that the use of a reduced pile unit weight for EB-I piles should be used with care, as it may lead to an unsafe pile design with respect to the pile normal force distribution. It is worth noting that this rationale is not restricted to the EB-I, but it generally applies for embedded FE models with a dimensionally reduced representation of Ω^p and overlapping subdomains (Granitzer et al., 2024d).

5 High-rise building foundation

The third validation exercise studies the EB-I performance employing the 21-storey Franklin Tower. Specifically, this study examines the influence of the NRC on the foundation settlements, simulation runtime and pile skin resistance; compare Section 2.3. Section 5.1 and Section 5.2 briefly describe the project and FE model details, followed by parametric studies presented in Section 5.3.

5.1 Case study: Franklin Tower

Figure 11 shows the around 80-m-high Franklin Tower, which is located adjacent to the Zürich Oerlikon train station. This stepped high-rise building is founded on a piled raft foundation formation, which has a rectangular shape of around 20 × 80 m with partial curvature to the north and is subjected to non-uniformly distributed eccentric loads (Bhartiya et al., 2024). The design of the tower foundation has been assisted by detailed FEA, with the aim to assess the effectiveness of various foundation measures and ensure structural integrity of deformation-sensitive perimeter constructions. The latter include, but are not restricted to, a shopping center with multiple basement levels, a pedestrian underpass and railway tracks. At a depth of about 30 m below the ground level, the Franklin Tower is additionally crossed by a sewer tunnel with a diameter of around 5 m. Interested readers may refer to Granitzer et al. (2024b) for details concerning the governing aspects driving the foundation design.

The subsoil conditions are characterized by several glacial-interglacial periods, in which basins and valleys of the Alpine region have been filled by lake and riverine sediments (Oberhollenzer et al., 2022). Specifically, the Franklin Tower is founded on alternating layers of fine-grained clayey-silty and silty-sandy soil with a varying degree of overconsolidation; see Figure 12A. A Moraine layer with a constant thickness of around 1.5 m forms the boundary between the fine-grained sediments and the underlying Molasse rock formation. As could be observed from Figure 12B, this Moraine boundary layer extends at a depth of 35–45 m in the project area and has a south-west to north-east descending gradient. This aspect has influenced the tunneling method employed for the sewer tunnel, originally excavated using both, mechanical as well as conventional tunnel driving techniques. The average groundwater level is around 5 m below the terrain, that is, significantly above the excavation base level; see Figure 11B.

Essentially, Granitzer et al. (2024b) report a satisfactory agreement of the measured (differential) foundation settlements with the original calculation model (Figure 12) involving SFEA piles and around 990,000 quadratic solid FEs. This evidence renders the original calculation model optimal for EB-I validation studies with a particular focus on the relative importance of the NRC; see Section 2.3. Key aspects of the numerical analysis scenario are addressed in the next subsection.

5.2 Finite element model details

Figure 12 shows the structural components, model dimensions and ground stratification of the analysis domain. The lateral excavation support is provided by secant pile walls and jet grouting columns, which are modeled as diaphragm walls with equivalent thickness ($t_{pile} = 0.9\,m$; $t_{col} = 1.5\,m$) and identical embedment length $L = 23.9\,m$. The retaining walls and sewer tunnel sections are assumed isotropic elastic, apart from tunnel Section 2, which is assigned with an anisotropic elastic material set to account for the reduced lining stiffness in the different coordinate directions due to segmental joints (Zdravkovic et al., 2005); see Figure 12B. The raft is placed at a depth of around 10 m below the ground surface (Figure 11) and constructed with a varying thickness to account for the occurrence of eccentric foundation loads ($q = 110 - 540\,kPa$); see Figure 12C.

As visually described in Figure 12C, the raft is resting on 170 piles ($L_{pile} = 11.0 - 14.0\,m$; $D_{pile} = 0.9\,m$; $\gamma_{pile} = 25\,kN/m^3$), which are modeled using both, the numerical SFEA benchmark and the EB-I with penalty, local and non-local NRC; see Figure 2. Additional simulations are carried out employing the EB-L formulation after Tschuchnigg and Schweiger (2015) to study the influence of the coupling domain geometry on the credibility of selected simulation results; cf. Section 1. Furthermore, different mesh refinement levels are considered to analyze the mesh size effect on the EB-I and EB-L predictions, respectively, whereas the number of solid FEs ranges from approximately 385,000 (coarse) to 790,000 (fine). In analogy to the FEA described in Section 4, the pile-raft contact associated with the EB-I and EB-L piles is established by employing the "perforated" modeling technique; cf. Figure 9. Likewise, all simulations are carried out under drained conditions. The constitutive behavior of the ground model units (see Figure 12A) is described using the HSS model, while the calculation phase sequence aligns with the real project phases. For brevity, a complete listing of the calibrated constitutive parameters and a comprehensive description of the calculation

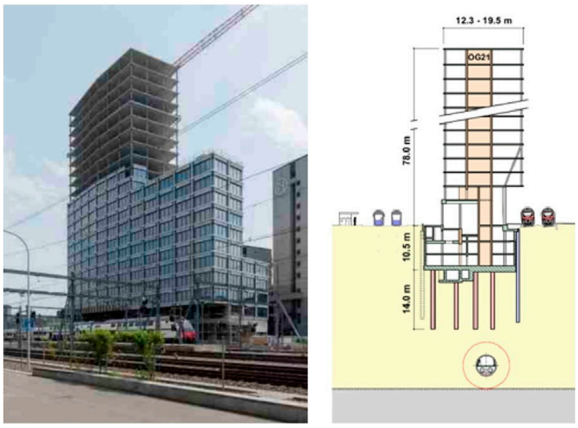

FIGURE 11
General view of Franklin Tower after completion of structural framework and partial façade installation, along with schematic cross-section (Granitzer et al., 2024b, modified).

phase sequence are omitted. Interested readers can refer to Schweiger et al. (2018) and Granitzer et al. (2024b) for details.

5.3 Finite element analysis

Figure 13 depicts the foundation settlement contours obtained with different pile modeling approaches (SFEA, EB-L, EB-I) and NRCs (penalty, local, non-local) in the final loading phase. Due to the varying raft thickness, and for reasons of consistency, the settlements are recovered from the mid-height of distinct raft foundation sections; see Figure 12C.

From the results, it can be inferred that all simulation results are consistent in the sense that the maximum settlements occur close to the raft center beneath raft foundation section B3 and the settlements gradually decrease towards the raft edges. This observation is not surprising, as this section is exposed to the maximum foundation load ($q = 540\,kPa$). Moreover, load-induced settlements evolving in close vicinity to the raft perimeter are, to some extent, suppressed by confinement effects of the permanent retaining walls on the piled raft foundation, giving them the role of "settlement reducers". A comparison with the original calculation model, involving SFEA piles, provides valuable insights into two important features associated with the EB-I and EB-L predictions. First, the relative difference of the settlements obtained with EB-I piles is smaller than when the piles are modeled with EB-Ls. Particular with respect to the maximum settlement values, relative merits of the EB-I predictions are striking. Overall, the EB-I simulations achieve a reasonable agreement with the original calculation model, except for the settlements obtained along the left retaining wall which are slightly overestimated. The second observation is that in this BVP the NRC has an insignificant influence on the load-settlement response of the piles. This numerical evidence is qualitatively consistent with the results of Granitzer et al. (2024c) presented in the context of single pile analyses and uniform soil conditions.

The next study assesses the influence of the pile modeling approach on the computational efficiency, with a particular focus on the NRC. For consistency, all simulations are conducted on a conventional workstation with 64-bit Windows 10 OS, Intel Core i7-7700K 4.2 GHz processor, 32 GB of RAM and a solid-state drive. It is important to notice that the total runtime documented in Table 1 incorporates the setup time for the pre-conditioner as well as the iteration time for solving the system of non-linear equations, and is obtained by running the simulations until the out-of-balance force is less than the default tolerated global error of 1%. The presented speedup ratio is computed as the total runtime of the EB-I and EB-L models, respectively, divided by the total runtime consumed by the original calculation model with SFEA piles.

With reference to the EB-I models, Table 1 indicates a significant decrease in runtime, particularly for the simulations carried out with the coarse mesh. This is manifested in speedup ratios of 3.25 – 3.87. Likewise, this observed tendency is reflected by the significantly reduced

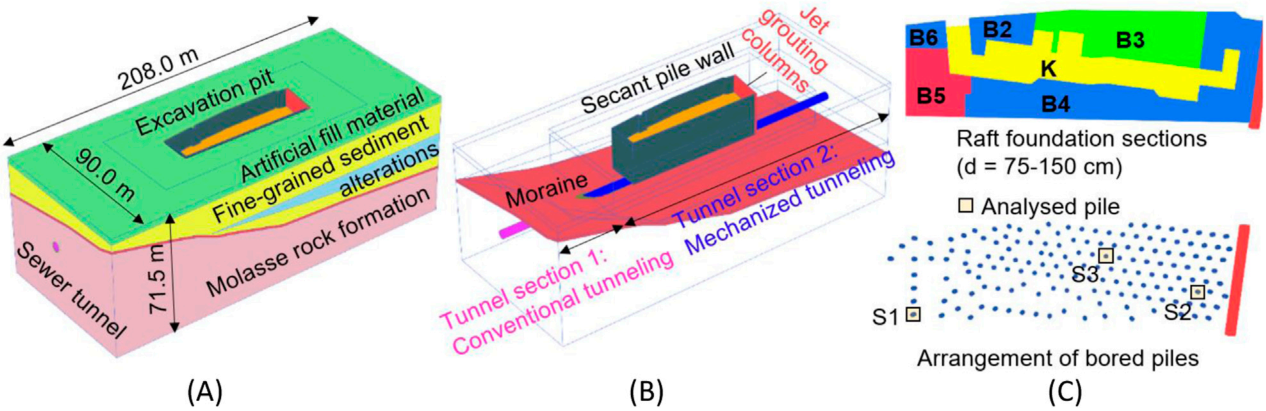

FIGURE 12
Description of original calculation model "Franklin Tower": **(A)** Model configuration and ground model; **(B)** sewer tunnel, excavation support and moraine layer; **(C)** pile arrangement layout.

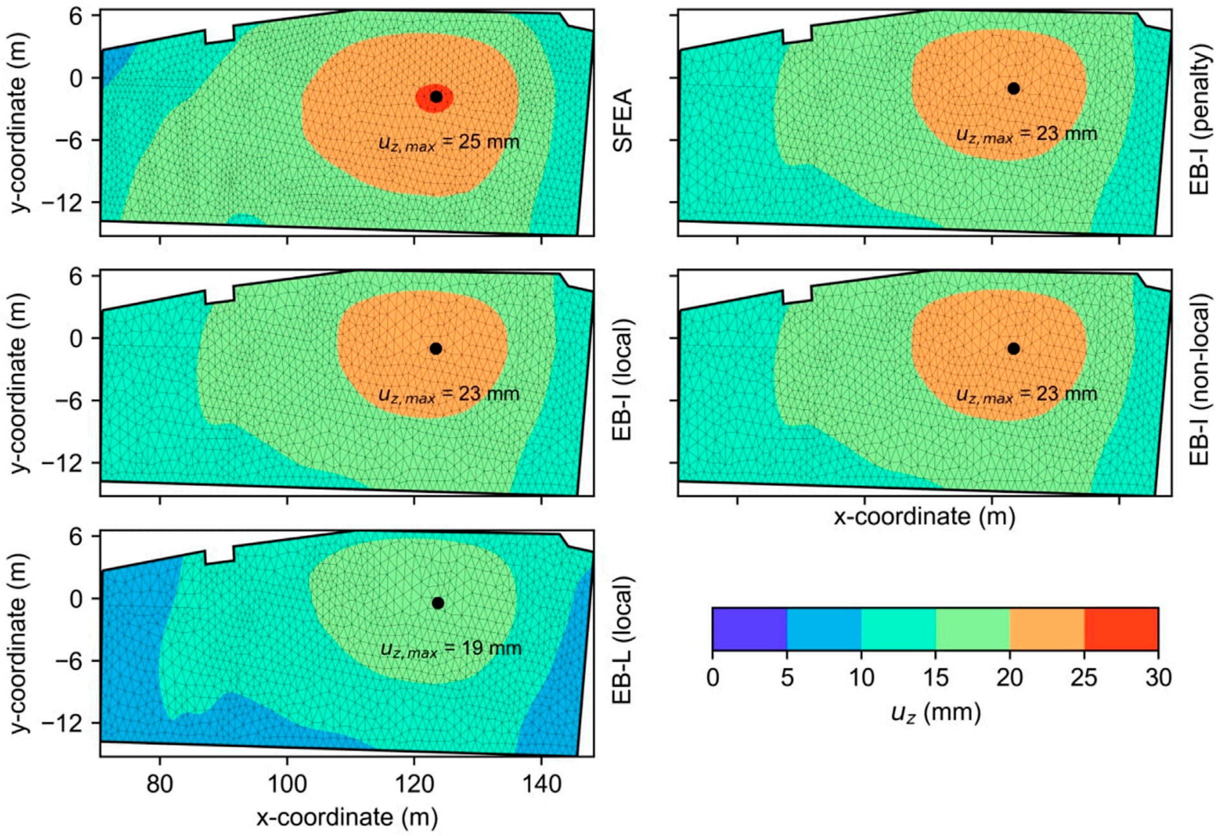

FIGURE 13
Influence of pile modeling approach and EB-I normal stress recovery technique on foundation settlement contours of the Franklin Tower raft after the final loading phase. The EB-L and EB-I results are presented with respect to the coarse mesh topology.

normalized runtime per iteration. However, due to the increased number of active DOFs, relative merits in terms of the computational costs are suppressed by employing the fine mesh topology, where the speedup ratios are reduced to 1.15 – 1.17. In all cases, the penalty and non-local NRC achieve slightly improved metrics compared to the local NRC. This tendency qualitatively aligns with the results reported in Granitzer et al. (2024c). Contrary to the EB-I models, the computational efficiency deteriorates in cases where the piles are modeled by means of the EB-L, that is, related speedup ratios (0.24 – 0.55) indicate that the total runtime exceeds those observed with SFEA piles, regardless of the adopted mesh topology. The numerical origin of this anomaly has been delineated based on eigenvalue analyses of the global stiffness matrix (Granitzer et al., 2024d). Specifically, this work demonstrates that an expansion of the interaction domain geometry from an interaction line (EB-L) to an interaction surface (EB-I) results in an improved conditioning of the global stiffness matrix and enhanced convergence rates.

To some extent, the improved numerical robustness associated with the EB-I is reflected in the skin traction profiles shown in Figure 14A. The latter are obtained from three different piles with varying lengths and positions; see Figure 12. Apparently, the EB-L predictions are prone to numerical oscillations, inherently caused by the non-smoothness of the relative displacement field along the interaction line; cf. Granitzer and Tschuchnigg (2023). This numerical obstacle is additionally amplified by the fine mesh (see Figure 14B), which indicates unrealistic negative skin traction values for the S2 pile, as opposed to EB-I predictions. These obstacles are clearly alleviated with the EB-I, which produces skin traction distributions that are relatively independent of the adopted mesh topology and NRC. Moreover, the EB-I has the ability to capture changes in the skin traction distribution induced by the inclined soil layer boundary; cf. Granitzer et al. (2024c). From this perspective, the results indicate that the EB-I can provide first order estimates of the skin traction profiles. Nevertheless, relative differences between the EB-I and the numerical SFEA benchmark close to the pile head (S2) and along limited shaft sections (S1, S3) are evident. To overcome related inconsistencies and enhance numerical fidelity, future EB-I developments could consider expanding the ACF reference data types to explicitly account for the computed skin traction profiles. Moreover, it may be advised to refine the interface constitutive relationship in Equation 2, originally adopted in modified form from Tschuchnigg (2013). However, these aspects are beyond the scope of the present paper and may be addressed in future research.

TABLE 1 Influence of NRC and mesh topology on total consumed runtime.

Model	Mesh	NRC	Time ($s \times 10^3$)	Speedup ratio (1)	# Steps (1)	# Iter (1)	Time/Iter (s)
SFEA			111.85	1.0	67	529	211.43
EB-L	coarse	local	204.86	0.55	470	4,142	49.46
	fine		459.37	0.24	369	4,578	100.34
EB-I	coarse	penalty	28.89	3.87	70	490	58.96
		local	34.39	3.25	74	491	70.04
		non-local	29.50	3.79	70	490	60.19
	fine	penalty	95.38	1.17	75	511	186.65
		local	96.95	1.15	73	531	182.58
		non-local	95.53	1.17	75	511	186.95

6 Conclusion

This work has been motivated by the growing demand of finite element formulations for the analysis of large-scale problems involving a high number of pile-type structures that strike a balance between adequate calculation fidelity and acceptable computational expense. Specifically, it extends previous works of the authors (Granitzer et al., 2024c; Granitzer et al., 2024d; Granitzer et al., 2024a), which have focused on the behavior of single piles under axial vertical loads, and for the first time provides insight into the performance of the developed embedded FE model with implicit interaction surface (EB-I) in geotechnical large-scale problems of practical relevance. These include a 3 x 3 capped pile group and the pile foundations of two case studies, namely the integral railway bridge Ems-Jade-Channel in Germany and the high-rise Franklin Tower in Switzerland. The following conclusions can be drawn from their analysis:

- Overall, the EB-I simulations capture the measurements and numerical benchmark predictions in terms of global foundation displacements, pile displacement profiles, bending moment and normal force distributions with high accuracy. Furthermore, it is found that the investigated normal stress recovery techniques produce comparable results. Contrary to previous studies, it should be noted that this numerical evidence is retained from cases with pronounced load eccentricity and combined vertical and horizontal loading.
- The credibility of EB-I predictions is, to some extent, influenced by the selection of the embedded interface constitutive model parameters and the pile unit weight. The former could be successfully calibrated using the automatic calibration framework (ACF) formulated in Granitzer et al. (2024a). The calibrated values documented in this work may serve as a valuable reference in cases where the EB-I simulations are conducted without ACF use. Moreover, it is highlighted that the use of embedded FE models, including the EB-I, leads to overlapping subdomains and requires a careful selection of the associated pile unit weight, which should be determined according to the analysis aims.
- The EB-I proves superior to embedded FE models with implicit interaction line in terms of runtime efficiency and skin traction profiles. In this light, it can be concluded that the EB-I has a relatively higher potential to capture the behavior of piles with insignificant installation effects. Nevertheless, to some extent, the results point out that the predicted skin friction mobilization is yet optimal. To provide more realistic predictions, future research should therefore focus on the formulation of more genuine interface constitutive models and refined contact discretization techniques, such as pioneered by Turello et al. (2017) and Goudarzi and Simone (2019), respectively. Although this work demonstrates the suitability of the developed EB-I for a number of relevant geotechnical application conditions, it should be pointed out that the validation process generally builds on ongoing activities that do not have a clearly defined completion point, as the correctness and accuracy cannot be demonstrated for all possible conditions and applications (Oberkampf et al., 2004); therefore, further understanding of the numerical performance under different application conditions will be instrumental to increase acceptance and move the developed EB-I forward to eventually harness its capabilities in routine practice. This may involve validation studies where the EB-I is employed for the modelling of pile anchors (Zheng et al., 2024b), retaining walls formed by rotating vertical piles (Zheng et al., 2024a), or the parametric analysis of deep foundations near slopes (Zhou et al., 2024).

Data availability statement

The raw data supporting the conclusions of this article will be made available by the authors, without undue reservation.

Author contributions

A-NG: Conceptualization, Methodology, Project administration, Software, Validation, Visualization, Writing–original draft. HF: Validation, Visualization,

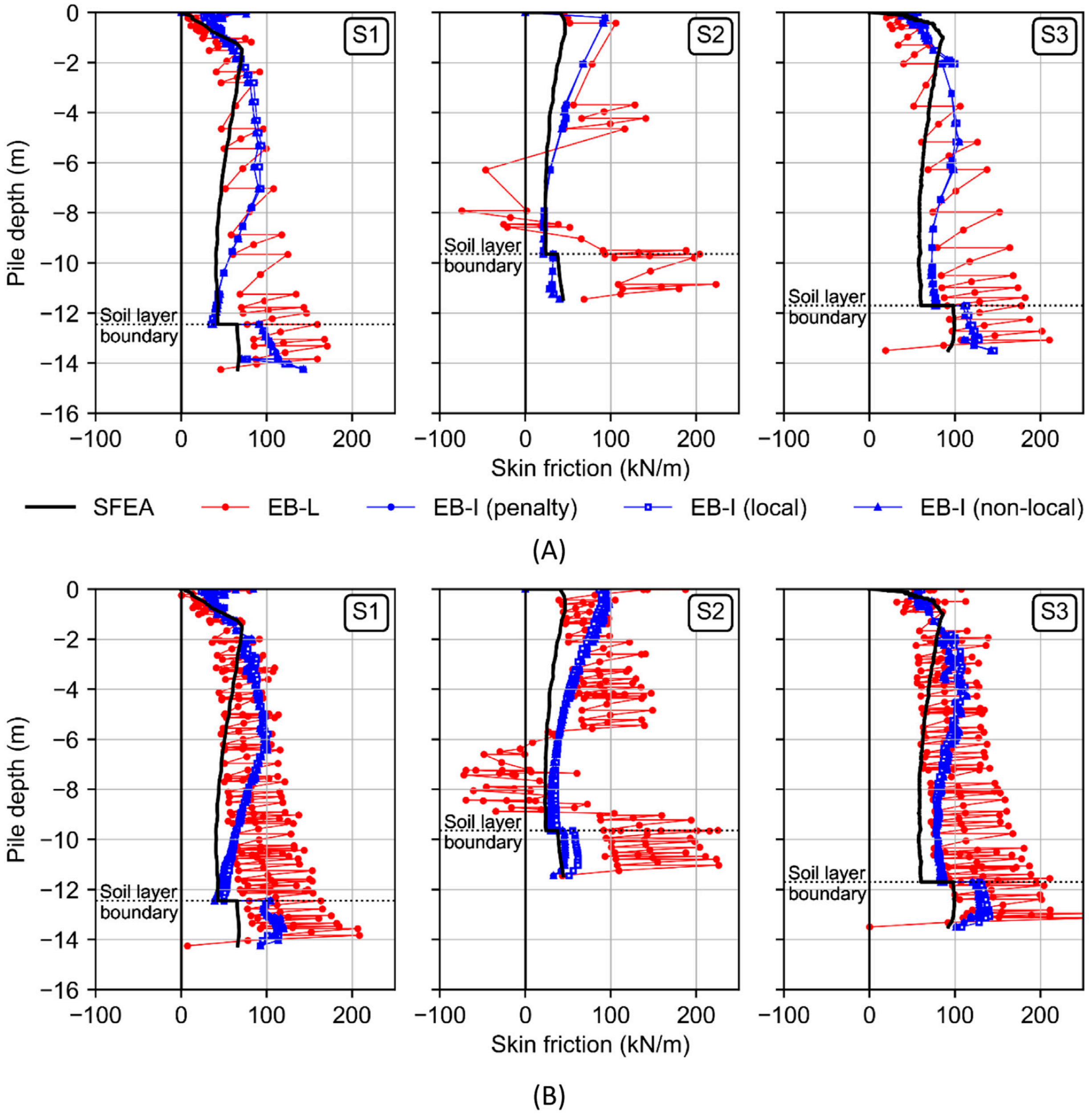

FIGURE 14
Influence of modeling approach and EB-I normal stress recovery technique on skin traction distribution of three different piles, evaluated with the **(A)** coarse and **(B)** fine mesh after final loading.

Writing–review and editing. JL: Validation, Visualization, Writing–review and editing. AS: Formal Analysis, Visualization, Writing–review and editing. FT: Supervision, Writing–review and editing.

Funding

The author(s) declare that no financial support was received for the research, authorship, and/or publication of this article.

Acknowledgments

The authors wish to thank Sven Kromminga, Max Käding and Marc Wenner from Marx Krontal Partner GmbH for providing the measurement data and figures concerning the integral bridge case study. The support provided by dsp Ingenieur + Planer AG and Christian Baudet with respect to the Franklin Tower case study is greatly acknowledged. We gratefully acknowledge the finicial support from the TU Graz Open Access Publishing Fund for providing the open access funding.

Conflict of interest

Author AS was employed by the company DB InfraGO AG.

The remaining authors declare that the research was conducted in the absence of any commercial or financial relationships that could be construed as a potential conflict of interest.

Publisher's note

References

Abu-Farsakh, M., Souri, A., Voyiadjis, G., and Rosti, F. (2018). Comparison of static lateral behavior of three pile group configurations using three-dimensional finite element modeling. *Can. Geotech. J.* 55, 107–118. doi:10.1139/cgj-2017-0077

Bentley Systems (2023). *Reference manual: plaxis 3D V2023.2.*

Benz, T., Schwab, R., and Vermeer, P. (2009). Small-strain stiffness in geotechnical analyses. *Bautechnik* 86, 16–27. doi:10.1002/bate.200910038

Bhartiya, P., Basu, D., and Chakraborty, T. (2024). Behavior of piled rafts in sand under nonuniform and eccentric loads. *Acta Geotech.* 19, 5315–5336. doi:10.1007/s11440-024-02247-6

Cai, X. (2003). "Overlapping domain decomposition methods," in *Advanced topics in computational partial differential equations*. Editors T. J. Barth, M. Griebel, D. E. Keyes, R. M. Nieminen, D. Roose, and T. Schlick (Berlin: Springer), 57–95.

CEN (2003). *Eurocode 1: actions on structures - Part 2: traffic loads on bridges. EN 1991-2:2003.* Brussels: European Committee for Standardization.

Cui, W., Wu, X., Potts, D. M., and Zdravković, L. (2023). Nonlocal strain regularisation for critical state models with volumetric hardening. *Comput. Geotechnics* 157, 105350. doi:10.1016/j.compgeo.2023.105350

Day, R. A., and Potts, D. M. (1994). Zero thickness interface elements—numerical stability and application. *Int. J. Numer. Anal. Meth. Geomech.* 18, 689–708. doi:10.1002/nag.1610181003

DB E and C (2019). *EÜ Ems-Jade-Channel: internal report concerning numerical simulations of static pile load tests.* Hannover.

DB ProjektBau GmbH (2013). *EÜ Ems-Jade-Channel: geotechnical report (main investigation).* Hannover.

DGGT (2014). *Recommendations on piling (EA-Pfähle)* (Berlin: Wilhelm Ernst and Sohn).

Di Laora, R., Sanctis, L. D., and Aversa, S. (2019). Bearing capacity of pile groups under vertical eccentric load. *Acta Geotech.* 14, 193–205. doi:10.1007/s11440-018-0646-5

Di Prisco, C., Flessati, L., and Porta, D. (2020). Deep tunnel fronts in cohesive soils under undrained conditions: a displacement-based approach for the design of fibreglass reinforcements. *Acta Geotech.* 15, 1013–1030. doi:10.1007/s11440-019-00840-8

Engin, H., Brinkgreve, R., and Septanika, E. (2007). "Improved embedded beam elements for the modelling of piles," in *Numerical models in geomechanics: proceedings of the 10th international symposium on numerical models in geomechanics*. Editor G. N. Pande (London: Taylor and Francis), 475–480.

Fellenius, B. H., and Altaee, A. (1995). Critical Depth: how it came into being and why it does not exist. *Geotech. Eng.* 113, 107–111. doi:10.1680/igeng.1995.27590

Franza, A., and Marshall, A. M. (2019). Centrifuge and real-time hybrid testing of tunneling beneath piles and piled buildings. *J. Geotechnical Geoenvironmental Eng.* 145, 1–10. doi:10.1061/(ASCE)GT.1943-5606.0002003

Franza, A., and Sheil, B. (2021). Pile groups under vertical and inclined eccentric loads: elastoplastic modelling for performance based design. *Comput. Geotechnics* 135, 104092. doi:10.1016/j.compgeo.2021.104092

Galavi, V., and Schweiger, H. F. (2010). Nonlocal multilaminate model for strain softening analysis. *Int. J. Geomech.* 10, 30–44. doi:10.1061/(ASCE)1532-3641(2010)10:1(30)

Ghofrani, A. (2018). *Development of numerical tools for the evaluation of pile response to laterally spreading soil.* Washington DC: University of Washington. Dissertation.

Goudarzi, M., and Simone, A. (2019). Discrete inclusion models for reinforced composites: comparative performance analysis and modeling challenges. *Comput. Methods Appl. Mech. Eng.* 355, 535–557. doi:10.1016/j.cma.2019.06.026

Granitzer, A., Tschuchnigg, F., Summerer, W., Galler, R., and Stoxreiter, T. (2021). Errichtung eines Eisenbahntunnels in Deckelbauweise über dem Hauptsammler West der Stadt Stuttgart/Construction of a railway tunnel above the main drainage tunnel of Stuttgart using the cut-and-cover method. *Bauingenieur* 96, 156–164. doi:10.37544/0005-6650-2021-05-40

Granitzer, A.-N., Leo, J., and Tschuchnigg, F. (2024a). Particle Swarm optimization of interface constitutive model parameters for embedded beam formulations. *Int. J. Geomech.* 24. in press. doi:10.1061/IJGNAI/GMENG-9429

Granitzer, A.-N., Stastny, A., Felic, H., Leo, J., Buss, C., and Tschuchnigg, F. (2024b). "Einfluss der Pfahlmodellierung bei FE-Analysen am Beispiel von zwei komplexen Großprojekten," in *14th Austrian geotechnical conference and vienna-terzaghi-lecture: proceedings*. Editors D. Adam and A. Hausenberger (Vienna: ÖIAV), 313–324.

Granitzer, A.-N., and Tschuchnigg, F. (2021). Practice-oriented validation of embedded beam formulations in geotechnical engineering. *Processes* 9, 1739–39. doi:10.3390/pr9101739

Granitzer, A.-N., and Tschuchnigg, F. (2023). "Finite element formulations for implicit beam-to-solid coupling: numerical obstacles and solution strategies," in *10th European conference on numerical methods in geotechnical engineering (NUMGE 2023): proceedings.* Editors L. Zdravkovic, A. Tsiampousi, D. Taborda, and S. Kontoe (Boca Raton: CRC Press), 1–6.

Granitzer, A.-N., Tschuchnigg, F., Felic, H., Bonnier, P., and Brasile, S. (2024c). Implementation and appraisal of stress recovery techniques for embedded finite elements with frictional contact. *Comput. Geotechnics* 172, 106457. doi:10.1016/j.compgeo.2024.106457

Granitzer, A.-N., Tschuchnigg, F., Hosseini, S., and Brasile, S. (2024d). Insight into numerical characteristics of embedded finite elements for pile-type structures employing an enhanced formulation. *Int. J. Numer. Anal. Meth. Geomech.* 48, 223–249. doi:10.1002/nag.3641

Hanisch, J., Katzenbach, R., and König, G. (2002). *Kombinierte pfahl-plattengründungen*. Berlin: Ernst and Sohn.

He, R., and Kaynia, A. M. (2024). Winkler spring coefficients for laterally loaded piles. *Comput. Geotechnics* 170, 106264. doi:10.1016/j.compgeo.2024.106264

Helwig, S. (2010). *Particle swarms for constrained optimization*. Nuremberg: University of Erlangen–Nuremberg. Dissertation.

Jauregui, R., and Silva, F. (2011). "Numerical validation methods," in *Numerical analysis - theory and application*. Editor J. Awrejcewicz (London: InTech Open), 155–174.

Jürgens, H., Vogel, P., Henke, S., and Grabe, J. (2022). Zur numerischen Berechnung der globalen Standsicherheit von Bauwerken im Boden. *Geotechnik* 45, 155–169. doi:10.1002/gete.202200003

Kaynia, A. M., and Kausel, E. (1991). Dynamics of piles and pile groups in layered soil media. *Soil Dyn. Earthq. Eng.* 10, 386–401. doi:10.1016/0267-7261(91)90053-3

Kishida, H., and Meyerhof, G. G. (1966). "Bearing capacity of pile groups under eccentric loads in sand," in *Proceedings of the 6th international conference on soil mechanics and foundation engineering*. Editor R. F. Legget (Toronto: University of Toronto Press), 270–274.

Lődör, K., and Balázs, M. (2018). "Finite element modelling of rigid inclusion ground improvement," in *Numerical methods in geotechnical engineering: proceedings of the 9th European conference on numerical methods in geotechnical engineering*. Editors A. S. Cardoso, J. L. Borges, P. A. Costa, A. T. Gomes, J. C. Marques, and C. S. Vieira (London: CRC Press), 1399–1406.

Marzouk, I., Granitzer, A.-N., Rauter, S., and Tschuchnigg, F. (2024). A case study on advanced CPT data interpretation: from stratification to soil parameters. *Geotech. Geol. Eng.* 42, 4087–4113. doi:10.1007/s10706-024-02774-9

Mendez, F. J., Pasculli, A., Mendez, M. A., and Sciarra, N. (2021). Calibration of a hypoplastic model using genetic algorithms. *Acta Geotech.* 16, 2031–2047. doi:10.1007/s11440-020-01135-z

Meyerhof, G. G., Yalcin, A. S., and Mathur, S. K. (1983). Ultimate pile capacity for eccentric inclined load. *J. Geotechnical Eng.* 109, 408–423. doi:10.1061/(ASCE)0733-9410(1983)109:3(408)

MKP (2020). *EÜ Ems-Jade-Channel: measurement concept and continuous technical monitoring: Marx krontal partner GmbH.* Weimar.

Ngo, D., and Scodelis, A. C. (1967). Finite element analysis of reinforced concrete beams. *ACI J.* 64, 152–163. doi:10.14359/7551

Ninić, J., Stascheit, J., and Meschke, G. (2014). Beam-solid contact formulation for finite element analysis of pile-soil interaction with arbitrary discretization. *Num Anal. Meth Geomech.* 38, 1453–1476. doi:10.1002/nag.2262

Oberhollenzer, S., Baldermann, A., Marte, R., Tahir, D. M. M., Tschuchnigg, F., Dietzel, M., et al. (2022). Microstructure development in artificially cemented, fine-grained soils. *Geosciences* 12, 333–417. doi:10.3390/geosciences12090333

Oberkampf, W. L., Trucano, T. G., and Hirsch, C. (2004). Verification, validation, and predictive capability in computational engineering and physics. *Appl. Mech. Rev.* 57, 345–384. doi:10.1115/1.1767847

Öchsner, A., and Merkel, M. (2018). *One-dimensional finite elements: an introduction to the FE method*. Basel: Springer Cham.

Oliveria, D., and Wong, P. K. (2011). Use of embedded pile elements in 3D modelling of piled-raft foundations. *Aust. Geomechanics J.* 46, 9–19.

Phillips, D. V., and Zienkiewicz, O. C. (1976). Finite element non-linear analysis of concrete structures. *Proc. Institution Civ. Eng.* 61, 59–88. doi:10.1680/iicep.1976.3503

Poulos, H. G. (2010). "High-rise building foundations—a limit state design approach," in *Art of foundation engineering practice*. Editor M. H. Hussein (Reston: ASCE), 501–516.

Poulos, H. G., and Davis, E. H. (1980). *Pile foundation and design*. New Jersey: John Wiley and Sons Inc.

Rajapakse, R. K. N. D. (1990). Response of an axially loaded elastic pile in a Gibson soil. *Géotechnique* 40, 237–249. doi:10.1680/geot.1990.40.2.237

Randolph, M. F., and Wroth, C. P. (1979). An analysis of the vertical deformation of pile groups. *Géotechnique* 29, 423–439. doi:10.1680/geot.1979.29.4.423

Sadek, M., and Shahrour, I. (2004). A three dimensional embedded beam element for reinforced geomaterials. *Num Anal. Meth Geomech.* 28, 931–946. doi:10.1002/nag.357

Schweiger, H. F., Tschuchnigg, F., and Oberhollenzer, S. (2018). *Franklin turm - Zürich: final project report*. Graz: Graz University of Technology.

Sheil, B. B., and McCabe, B. A. (2016). An analytical approach for the prediction of single pile and pile group behaviour in clay. *Comput. Geotechnics* 75, 145–158. doi:10.1016/j.compgeo.2016.02.001

Sheil, B. B., McCabe, B. A., Comodromos, E. M., and Lehane, B. M. (2019). Pile groups under axial loading: an appraisal of simplified non-linear prediction models. *Géotechnique* 69, 565–579. doi:10.1680/jgeot.17.r.040

Smulders, C. M., Hosseini, S., and Brinkgreve, R. (2019). "Improved embedded beam with interaction surface," in *Proceedings of the 17th European conference on soil mechanics and geotechnical engineering*. Editors H. Sigursteinsson, S. Erlingsson, and B. Bessason (Reykjavík: COC), 1048–1055.

Stastny, A., Knittel, L., Meier, T., and Tschuchnigg, F. (2024). Experimental determination of hypoplastic parameters and cyclic numerical analysis for railway bridge backfills. *Acta Geotech.* doi:10.1007/s11440-024-02312-0

Stastny, A., Stein, R., and Tschuchnigg, F. (2022). "Long-term monitoring of the transition zone of an integral railway bridge in Germany," in *Field measurements in geomechanics*, 1–7. ISSMGE TC220.

Staubach, P., Machaček, J., and Wichtmann, T. (2022). Novel approach to apply existing constitutive soil models to the modelling of interfaces. *Int. J. Numer. Anal. Meth. Geomech.* 46, 1241–1271. doi:10.1002/nag.3344

Staubach, P., Tschirschky, L., Machaček, J., and Wichtmann, T. (2023). Monopile installation in clay and subsequent response to millions of lateral load cycles. *Comput. Geotechnics* 155, 105221. doi:10.1016/j.compgeo.2022.105221

Steinbrecher, I., Hagmeyer, N., Meier, C., and Popp, A. (2022a). *A consistent mixed-dimensional coupling approach for 1D Cosserat beams and 2D solid surfaces*. Preprint, submitted October 28, 2022. doi:10.48550/arXiv.2210.16010

Steinbrecher, I., Mayr, M., Grill, M. J., Kremheller, J., Meier, C., and Popp, A. (2020). A mortar-type finite element approach for embedding 1D beams into 3D solid volumes. *Comput. Mech.* 66, 1377–1398. doi:10.1007/s00466-020-01907-0

Steinbrecher, I., Popp, A., and Meier, C. (2022b). Consistent coupling of positions and rotations for embedding 1D Cosserat beams into 3D solid volumes. *Comput. Mech.* 69, 701–732. doi:10.1007/s00466-021-02111-4

Stewart, J. F., and Kulhawy, F. H. (1981). "Interpretation of uplift load distribution data," in *Proceedings of the 10th international conference on soil mechanics and foundation engineering* (Stockholm: A.A. Balkema), 277–280.

Tradigo, F., Pisanò, F., and Di Prisco, C. (2016). On the use of embedded pile elements for the numerical analysis of disconnected piled rafts. *Comput. Geotechnics* 72, 89–99. doi:10.1016/j.compgeo.2015.11.005

Trochanis, A. M., Bielak, J., and Christiano, P. (1991). Three-dimensional nonlinear study of piles. *J. Geotechnical Eng.* 117, 429–447. doi:10.1061/(ASCE)0733-9410(1991)117:3(429)

Truty, A. (2023). Nonlocal FEM modeling of piles as beam elements embedded within 3D continuum. *Eng. Struct.* 277, 115460. doi:10.1016/j.engstruct.2022.115460

Tschuchnigg, F. (2013). *3D finite element modelling of deep foundations employing an embedded pile formulation*. Graz: Graz University of Technology.

Tschuchnigg, F., and Schweiger, H. F. (2010). "Study of a complex deep foundation system using 3D Finite Element analysis," in *Numerical methods in geotechnical engineering: proceedings of the seventh European conference on numerical methods in geotechnical engineering, trondheim, Norway, 2-4 june 2010*. Editors S. Nordal and T. Benz (Leiden: CRC Press), 40–46.

Tschuchnigg, F., and Schweiger, H. F. (2013). Comparison of deep foundation systems using 3D finite element analysis employing different modeling techniques. *Geotech. Eng.* 44, 40–46.

Tschuchnigg, F., and Schweiger, H. F. (2015). The embedded pile concept – verification of an efficient tool for modelling complex deep foundations. *Comput. Geotechnics* 63, 244–254. doi:10.1016/j.compgeo.2014.09.008

Turello, D. F., Pinto, F., and Sánchez, P. J. (2016). Embedded beam element with interaction surface for lateral loading of piles. *Num Anal. Meth Geomech.* 40, 568–582. doi:10.1002/nag.2416

Turello, D. F., Pinto, F., and Sánchez, P. J. (2017). Three dimensional elasto-plastic interface for embedded beam elements with interaction surface for the analysis of lateral loading of piles. *Num Anal. Meth Geomech.* 41, 859–879. doi:10.1002/nag.2633

Turello, D. F., Pinto, F., and Sánchez, P. J. (2019). Analysis of lateral loading of pile groups using embedded beam elements with interaction surface. *Num Anal. Meth Geomech.* 43, 272–292. doi:10.1002/nag.2863

Waas, G., and Hartmann, H. G. (1984). "Seismic analysis of pile foundations including pile-soil-pile interaction," in *Proceedings of the 8th world conference on earthquake engineering, EERI* (Englewood Cliffs: Prentice-Hall), 55–62.

Watcharasawe, K., Jongpradist, P., Kitiyodom, P., and Matsumoto, T. (2021). Measurements and analysis of load sharing between piles and raft in a pile foundation in clay. *Geomechanics Eng.* 24, 559–572. doi:10.12989/GAE.2021.24.6.559

Williamson, M. G., Mair, R. J., Devriendt, M. D., and Elshafie, M. Z. E. B. (2017). Open-face tunnelling effects on non-displacement piles in clay – part 2: tunnelling beneath loaded piles and analytical modelling. *Géotechnique* 67, 1001–1019. doi:10.1680/jgeot.SIP17.P.120

Zdravkovic, L., Potts, D. M., and St John, H. D. (2005). Modelling of a 3D excavation in finite element analysis. *Géotechnique* 55, 497–513. doi:10.1680/geot.2005.55.7.497

Zheng, G., Guo, Z., Zhou, H., and He, X. (2024a). Design method for wall deformation and soil movement of excavations with inclined retaining walls in sand. *Int. J. Geomech.* 24. doi:10.1061/IJGNAI.GMENG-9029

Zheng, G., Guo, Z., Zhou, H., Tan, Y., Wang, Z., and Li, S. (2024b). Multibench-retained excavations with inclined–vertical framed retaining walls in soft soils: observations and numerical investigation. *J. Geotechnical Geoenvironmental Eng.* 150. doi:10.1061/JGGEFK.GTENG-11943

Zhou, H., Zhang, J., Yu, X., Hu, Q., Zheng, G., Xu, H., et al. (2024). Stochastic bearing capacity and failure mechanism of footings placed adjacent to slopes considering the anisotropic spatial variability of the clay undrained strength. *Int. J. Geomech.* 24. doi:10.1061/IJGNAI.GMENG-9136

Glossary

1D, 2D, 3D	One-dimensional, two-dimensional, three-dimensional
ACF	Automatic calibration framework proposed by Granitzer et al. (2024a)
BVP	Boundary value problem
c’	Soil cohesion
DOF	Degree of freedom
$\mathbf{D_{pile}}$	Pile diameter
e	Eccentric distance of point load
$\mathbf{E_{pile}}$	Pile Young’s modulus
$\mathbf{E_{RSE}}$	Relative squared error
$\mathbf{E_{50}^{ref}}$	Deviatoric hardening modulus in HSS model at reference pressure
EB-I	Embedded FE model with implicit interaction surface
EB-L	Embedded FE model with implicit interaction line
$\mathbf{E_{oed}^{ref}}$	Stiffness for primary oedometer loading in HSS model at reference stress
$\mathbf{E_{ur}^{ref}}$	Stiffness for un- and reloading in HSS model at reference stress
FE	Finite element
FEA	Finite element analysis
$\mathbf{F_z}$	Vertical pile head load
g, q	Permanent and traffic load
$\mathbf{G_0^{ref}}$	Initial soil shear stiffness at small strains in HSS model at reference pressure
$\mathbf{G_{soil}}$	Current soil shear stiffness sampled at TSFE integration points
$\mathbf{\bar{G}_{TSFE}}$	Current soil shear stiffness averaged over integration points of TSFE
H	Mapping function matrix
HSS	Hardening Soil Small constitutive model after Benz et al. (2009)
K	Embedded interface stiffness matrix
$\mathbf{L, L_{pile}}$	Pile and embedment length
m	Power index controlling stress dependency of soil stiffness in HSS model
M, N	Pile bending moment and normal force
NRC	Normal stress recovery technique
POP	Pre-overburden pressure
PSO	Particle Swarm Optimization
$\mathbf{p_{ref}}$	Reference stress
$\mathbf{R_{inter}}$	Interface shear strength reduction factor
$\mathbf{R_{pile}}$	Pile radius
$\mathbf{R_{inter}}$	Interface shear strength reduction factor
s	Time metric seconds
$\mathbf{S_0, S_1}$	Start and end of first summer cycle
SFEA	Standard finite element approach for the modeling of piles
$\mathbf{t_{pile}, t_{col}}$	Equivalent thickness of secant pile wall and jet grouting columns
$\mathbf{\tilde{t}}$	Skin traction vector with tangential $(\tilde{t}_2, \tilde{t}_3)$ and normal components with respect to $\mathbf{\tilde{x}}_i$
TSFE	Target solid finite element
$\mathbf{\hat{u}_b}$	Vector containing translation DOFs of beam FE node
$\mathbf{\tilde{u}_b, \tilde{u}_{rel}, \tilde{u}_s}$	Beam, relative and solid displacement vector at $\mathbf{\tilde{x}}_i$
$\mathbf{u_x}$	Horizontal displacement obtained by means of laser distance measurements
$\mathbf{u_z}$	Dirichlet boundary condition imposed in vertical *z*-direction on pile head
$\mathbf{x, x_{opt}}$	(Optimal) parameter vector involving Γ_b, Γ_s
$\mathbf{\tilde{x}_i}$	Coupling point
$\gamma(\cdot)$	Unit weight
$\gamma_{0.7}$	Shear strain in HSS model at which soil shear stiffness decays to $0.722 \cdot G_0$
$\mathbf{\Gamma_b, \Gamma_s}$	Embedded interface stiffness multipliers associated with EB-I base and shaft
$\mathbf{\Gamma_c}$	Coupling domain
$\mathbf{\Delta T}$	Difference in temperature measured at integral bridge superstructure
$\boldsymbol{\hat{\theta}_b}$	Vector containing rotational DOFs of beam FE node
$\boldsymbol{\theta_y}$	Rotation angle over y-axis
$\nu(\cdot)$	Poisson’s ratio
$\boldsymbol{\tilde{\sigma}_n'}$	Effective normal stress magnitude at $\mathbf{\tilde{x}}_i$
$\boldsymbol{\varphi'}$	Effective friction angle
$\boldsymbol{\psi}$	Dilatancy angle
$\mathbf{\Omega^p}$	Pile domain
$\mathbf{\Omega^s}$	Solid domain